Geochemistry Geophysics Geosystems G3
AN ELECTRONIC JOURNAL OF THE EARTH SCIENCES
Published by AGU and the Geochemical Society

Article
Volume 5, Number 2
10 February 2004
Q02003, doi:10.1029/2003GC000626
ISSN: 1525-2027

Hydrothermal venting at Vailulu'u Seamount: The smoking end of the Samoan chain

H. Staudigel
Scripps Institution of Oceanography, University of California, San Diego, La Jolla, California 92093, USA (hstaudigel@ucsd.edu)

S. R. Hart
Woods Hole Oceanographic Institution, Woods Hole, Massachusetts 02543, USA (shart@whoi.edu)

A. A. P. Koppers and C. Constable
Scripps Institution of Oceanography, University of California, San Diego, La Jolla, California 92093, USA (akoppers@ucsd.edu; cconstable@ucsd.edu)

R. Workman and M. Kurz
Woods Hole Oceanographic Institution, Woods Hole, Massachusetts 02543, USA (rworkman@whoi.edu; mkurz@whoi.edu)

E. T. Baker
Pacific Marine Environmental Laboratory, National Oceanic and Atmospheric Administration, Seattle, Washington 98115, USA (edward.baker@noaa.gov)

[1] The summit crater of Vailulu'u Seamount, the youngest volcano in the Samoan chain, hosts an active hydrothermal system with profound impact on the ocean water column inside and around its crater (2 km wide and 407 m deep at a 593 m summit depth). The turbidity of the ocean water reaches 1.4 NTU, values that are higher than in any other submarine hydrothermal system. The water is enriched in hydrothermal Mn (3.8 ppb) and ^{3}He (1×10^{-11} cc/g) and we measured water temperature anomalies near the crater floor up to 0.2°C. The hydrothermal system shows complex interactions with the ocean currents around Vailulu'u that include tidally-modulated vertical motions of about 40–50 m, and replenishment of waters into the crater through breaches in the upper half of the crater wall. Inside and outside potential density gradients suggest that hydrothermal venting exports substantial amounts of water from the crater ($1.3 \pm 0.2 \times 10^8$ m^3/day), which is in good agreement with fluxes obtained from a tracer release experiment inside the crater of Vailulu'u (0.8×10^8 m^3/day [*Hart et al.*, 2003]). This mass flux, in combination with the differences in the inside and outside crater temperature, yields a power output of around 760 megawatts, the equivalent of 20–100 MOR black smokers. The Mn output of 300 kg/day is approximately ten times the output of a single black smoker.

Components: 12,276 words, 10 figures, 3 tables.

Keywords: Hydrothermal; seamount; hot spots.

Index Terms: 4832 Oceanography: Biological and Chemical: Hydrothermal systems; 9355 Information Related to Geographic Region: Pacific Ocean; 3015 Marine Geology and Geophysics: Heat flow (benthic) and hydrothermal processes.

Received 28 August 2003; **Accepted** 6 November 2003; **Published** 10 February 2004.

Staudigel, H., S. R. Hart, A. A. P. Koppers, C. Constable, R. Workman, M. Kurz, and E. T. Baker (2004), Hydrothermal venting at Vailulu'u Seamount: The smoking end of the Samoan chain, *Geochem. Geophys. Geosyst.*, *5*, Q02003, doi:10.1029/2003GC000626.

1. Introduction

[2] Submarine hydrothermal systems are amongst the most fundamental features associated with the cooling of the earth. The most abundant and volumetrically significant fraction of these hydrothermal systems are located at the mid-ocean ridges, but they also occur at isolated submarine volcanoes in intraplate or arc settings. In total, these submarine hydrothermal systems play a key role in buffering the chemical and isotopic composition of seawater [*Elderfield and Schultz*, 1996; *Mottl and Wheat*, 1994], in modifying the chemical composition of the oceanic crust before it is recycled at subduction zones [*Hart and Staudigel*, 1982; *Staudigel et al.*, 1995] and in providing a habitat for deep and extreme life [*Hessler and Kaharl*, 1995; *Jannasch*, 1995].

[3] This paper presents results from the hydrothermal system of Vailulu'u seamount, an active intraplate volcano on the eastern end of the Samoan volcanic chain. These results offer insights into critical unknowns of submarine hydrothermal systems, the nature and size of thermal and chemical fluxes, and the coupling between hydrothermal systems and the oceans. Vailulu'u seamount is well suited for addressing these problems since: (1) It has a very robust hydrothermal system, with some of the densest submarine hydrothermal plumes observed anywhere in the oceans and large chemical and thermal fluxes; (2) Its summit crater has a geometry that focuses and confines hydrothermal flow; (3) Steep thermal gradients at summit depth allow constraints on vertical heave of the oceans that plays a critical role in plume-ocean interaction and the ventilation of the crater.

[4] This study of the Vailulu'u hydrothermal system is based on exploratory work that we "piggybacked" to the deployment and recovery of five Ocean Bottom Hydrophones using the US Coast Guard Icebreakers Polar Star and Polar Sea. These exploratory efforts yielded a detailed view of the hydrothermal system, despite the fact that this work was not specifically designed for this purpose and that icebreakers without dynamic positioning are not ideal platforms for laying out detailed surveys on a narrow, cratered volcano, compromising the layout of our hydrocasts, but not prohibiting us from determining the basic distribution of temperature, salinity and density gradients and hydrothermal particulates in and around the crater. This allowed us determine consistent hydrothermal fluxes using two independent methods, a fluorescent tracer release experiment [*Hart et al.*, 2003], and through a steady state water import model presented here, based on the diverging density and temperature trends inside and outside the crater.

[5] As a byproduct of the hydrophone deployments we obtained one-year temperature records at three sites on the crater rim and one on the crater floor. These records offered interesting insights into the hydrothermal - oceanographic setting. For example, they revealed substantial temperature variations with periods ranging from tidal to several months, allowing us to demonstrate an average 50m tidal heave of the water in the volcano summit region. Phase delays (i.e., the differences in arrival times) of the long period temperature variations (>5 days) at crater rim sites suggest westerly ocean currents. Tidal heaves result in pulsed deep water import into the crater during tidal highs, and ocean currents appear to deflect the hydrothermal plume into the enclosed eastern portion of the crater.

[6] However, despite the rather detailed knowledge of this hydrothermal system, many aspects remain unexplored, such as the type and location of hydrothermal vents or the interaction with the biosphere. Much work remains, but it is quite clear that Vailulu'u displays a very active hydrothermal system with thermal fluxes that are similar to volcanoes on mid-ocean ridge systems. The high fluxes and easy access make Vailulu'u an impor-

tant candidate for a natural laboratory in the study of submarine hydrothermal systems.

2. Data Acquisition and Methods

[7] In this study, we use hydrographic data and water samples obtained during two field seasons at Vailulu'u Seamount, one in March/April 2000, and the other in April 2001, aboard the U.S. Coast Guard Icebreaker Polar Star and Polar Sea, respectively. We used a SeaBird 911 conductivity-temperature-depth-optical (CTDO) package to obtain water samples and collect hydrographic and optical profiles. Accuracy of the SBE 911 include 0.0003 S/m for salinity, 0.001°C for temperature, and 0.015% for pressure (http://www.seabird.com/products/spec_sheets/911data.htm). We used the same WET Labs light backscattering sensor (LBSS) both years to measure the relative mass concentration of suspended particulate matter in terms of nephelometric turbidity units (NTU). NTU values were determined by calibration with standard particulate suspensions [*Hart et al.*, 2000; *Baker et al.*, 2001]. Most deployments were carried out from the icebreakers in a free-drift tow-yo mode. All the hydrographic data, and details on data reduction, are given in appendix A. We also analyzed 36 filtered water samples from the 2000 and 2001 cruises for Mn concentrations by ICP-MS and 19 "copper-tube" samples for ^{3}He concentrations. Data and details of the analyses are given in appendix B.

[8] We used "Vemco®" temperature recorders to measure hourly, in-situ temperatures at four sites for a 377 day period beginning 03/24/2000 (08:00 GMT); these sites are also locations of hydrophone deployments for which data will be decribed elsewhere. The temperature recorder/hydrophone packages floated approximately two meters above their seafloor anchors. Each site was named after Polynesian gods: Mafui'e was positioned on the crater floor, whereas Sasa'umani (Sasa), Fe'e and Lefaleilelagi (Lefa) were deployed along the crater rim (Figure 1). The Mafui'e site carried a second logger which sampled at a 5-minute rate for 38 days, beginning 05/01/2000 (00:00 GMT). The resolution of temperature measurements is 0.015°C, with an accuracy of 0.1°C. The inter-comparison of the two crater-floor instruments is better than 0.02°C, and the measurements are consistent with temperature measurements made with the CTD temperature probe. All temperature data, calibrations and some basic statistics are given in Electronic Data Supplement 2.

[9] In addition, we carried out a dye tracer-release experiment in 2001, which is described in detail in [*Hart et al.*, 2003]; 20kg of fluorescein dye was released in a point source 30 m above the crater floor, in the north-central portion of the crater (Figure 1). The dispersal of the dye was tracked for four days to determine the vertical and horizontal dispersion velocities.

2.1. Physical Setting

[10] Vailulu'u forms an independent volcanic edifice located at the easternmost end of the Samoan volcanic chain, and is linked to Ta'u Island by a 3000 m deep ridge (Figure 1). Vailulu'u volcano rises approximately 4400 m above the surrounding ocean floor, to a water depth of only 593 m (named Rockne Seamount when first discovered [*Johnson*, 1984]). Its summit displays a 2 km wide, 400 m deep crater which hosts a very active hydrothermal system [*Hart et al.*, 2000]. The crater rim is variable in elevation, with three summits and breaches. The shallowest peak, in the west, is bound by the two deepest breaches, one in the NW (795 m) and another one in the SE (764 m; Figure 1). In Figure 2a, we describe the crater in terms of its depth-volume and depth-breach area, whereby the total fraction of the breached crater circumference is zero at depths below 795 m, and increases to 100% at the summit depth, where there is no physical obstacle left for the circulation of external water. The crater volume is 905×10^6 m^3, determined as the volume encompassed by the enclosed and breached crater circumference to the summit depth; the enclosed crater volume is 38% of this value.

[11] The breaches are unevenly distributed and not equally sized. The NW breach is the deepest and largest, opening up the crater to any external water circulation above a depth of 795 m. It remains the

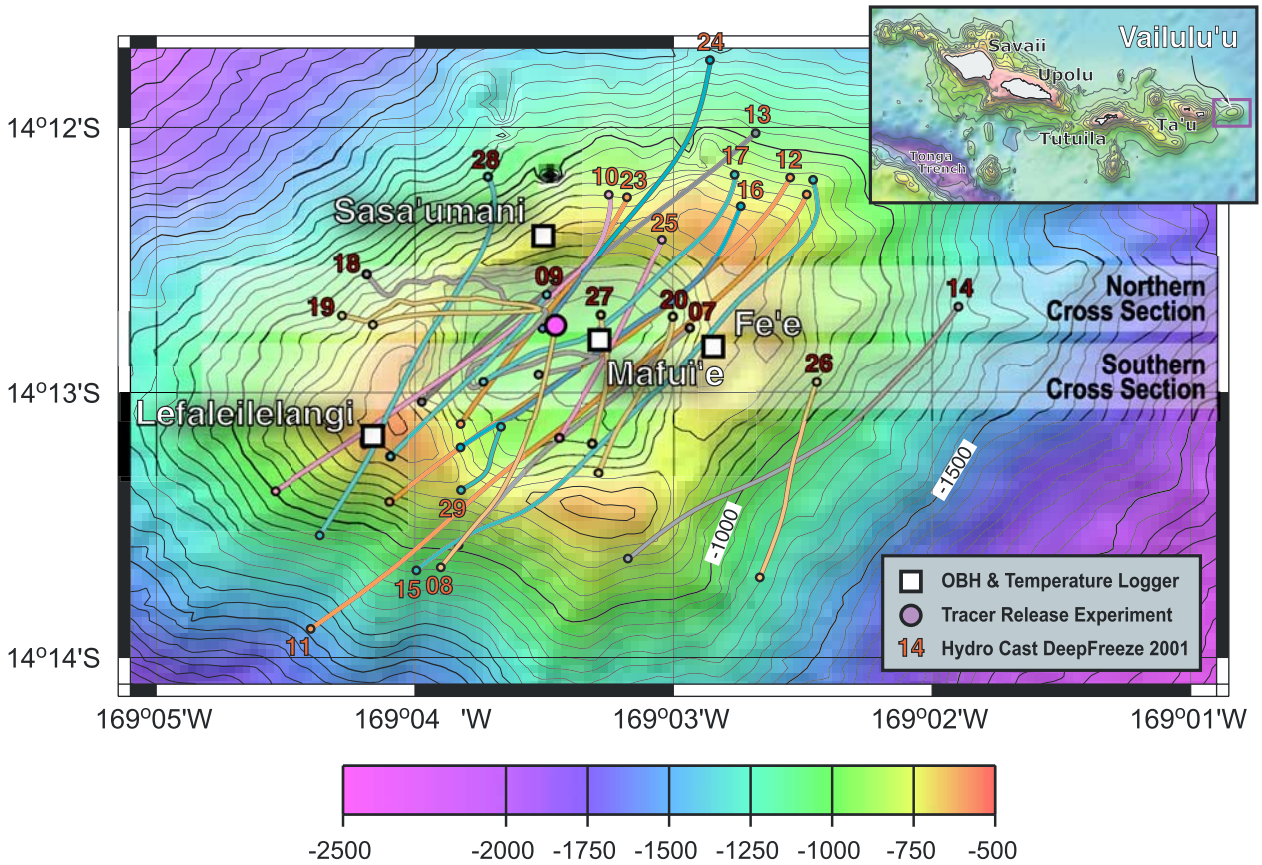

Figure 1. Map of the summit crater region of Vailulu'u seamount with numbered CTDO hydrocast tracks (appendices A and B). Open squares indicate location of temperature recorders attached to ocean bottom hydrophones with their respective names (after Polynesian gods, appendix 2). Lightly shaded areas (''Northern Cross section'' and ''Southern Cross Secton'') intersect tow-yo tracks projected on two east-west sections through the crater in Figure 7.

only breach to a water depth of 763 m, above which the SE breach opens. Opposite to the SE breach is the wide sill of the SW breach, at a depth of 730 m. The total breached area below 730 m is only 5% of the crater circumference, with the NW breach contributing 2/3 of this area (Figure 2a). However, as shown below, opening only 5% of the crater circumference is sufficient to make water column properties uniform between the inside and the outside of the crater.

[12] The water column in and above the crater may be divided into three major depth ranges based on the extent of crater breach area at a given depth: (1) the open ocean (''OO'') above the shallowest summit at 593 m, (2) the underlying breached crater down to the deepest breach level at 795 m, and (3) the completely enclosed crater interior down to a depth of 1000 m. Below, we have further divided the breached and the isolated zones of the crater into two distinct regions each, based on the nature of the potential temperature and density profiles.

2.2. Water Column Properties/Profiles

[13] The summit region of Vailulu'u is located at relatively shallow water depth, with steep gradients in hydrographic parameters that show substantial variation with depth and as a function of location and time. In Figures 2b and 2c, we have plotted all our hydrographic profiles, separated by locations within and outside the crater perimeter. Salinity, temperature and potential density all display steeper gradients above and outside the crater than inside the crater. The wide range of values shows the

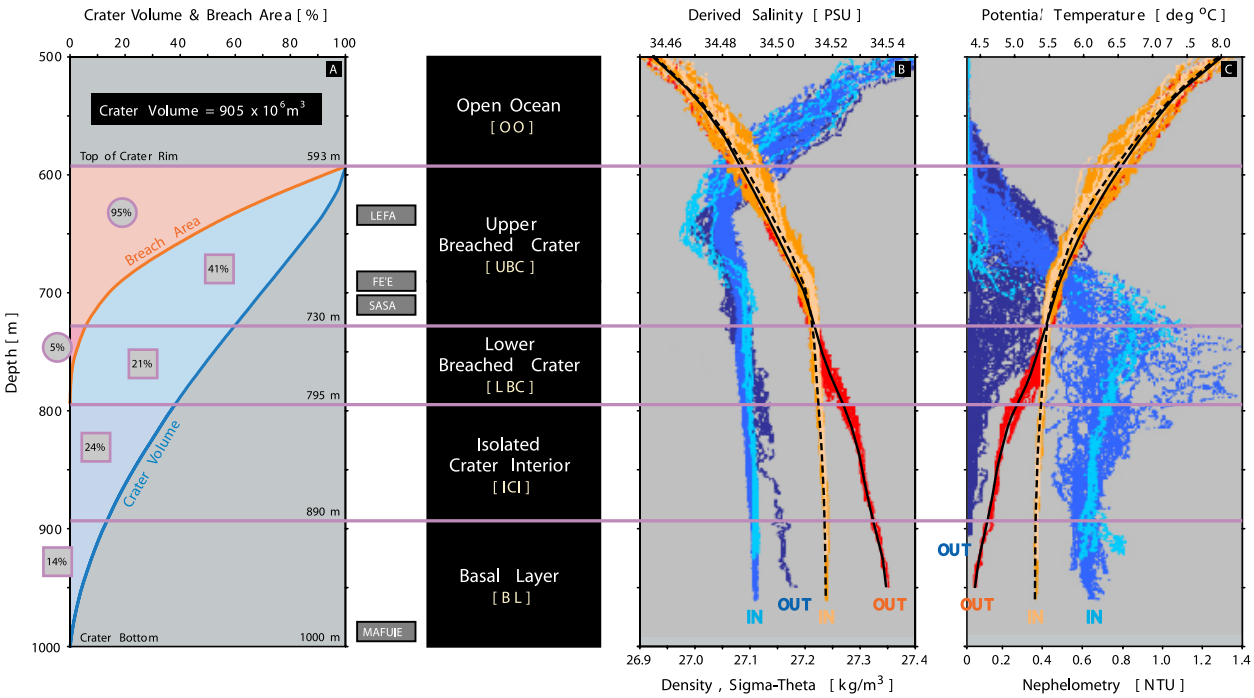

Figure 2. Overall physical and water property characteristics as a function of depth in the Vailulu'u crater region. In the "Crater Volume & Breach Area" panel, we plotted the depth relationships of cumulative crater volume within the circumference of the crater rim, and the fraction of the crater rim (linear distance) that is open to circulation. The deepest point of the crater floor is at 1020 m and 38% of the total crater volume is located below the deepest breach at 795 m water depth (data on volumes and breach area are from appendix B). The breached crater volume extends between 594–795 meters water depth. In the right-hand panels, salinity and nephelometry are in blue symbols, and temperature and density are in red/orange symbols; dark colors indicate the steady state ("T1" in insert of Figure 3), and light colors show the results of a series of profiles obtained at a time when much of the particulate matter in the upper UBC appeared to have been washed out ("T2"in insert of Figure 3). Salinity, temperature and potential density display steeper gradients above and outside the crater than inside the crater. Particulates show a gradual increase from Open Ocean depths to the LBC, and moderately but generally high values in the ICI and MBL. Depth of temperature records are indicated at the right-hand side of Figure 2a.

extreme variability of the water column, in particular at depths shallower than 650 m, both for profiles within and outside the crater. This large scatter at shallow depths is probably due to shallow ocean dynamics within steep gradients in hydrographic parameters, as well as the to-be-expected complex water circulation around the summit of Vailulu'u. Salinities, potential densities and temperatures at the 1000 m deep crater floor are similar to exterior values at depths of 760–800 m. In this depth range the crater has only one major breach (in the NW) and, therefore, this breach must play a crucial role in the delivery of waters to the crater floor.

[14] Salinity around the summit decreases rapidly with depth, reaches a minimum at 650 m water depth and slowly increases again with depth (note the expanded scale and resulting scatter). The coincidence of the salinity minimum and the approximate summit water depth is not causally related, since a similar salinity minimum is also apparent in profiles 50 km away from the volcano.

[15] Potential temperature shows steep decreases with depth in the upper part of the profiles and substantially smaller gradients at greater water depths; potential density gives a mirror-image of the temperature variations, inside and outside the crater. Individual temperature and density profiles scatter substantially, in particular in the shallowest and steepest parts of the curves, with a significant overlap between inside and outside profiles throughout the entire breached crater depth range (593–795 m). Averaged temperature and density profiles, however, are indistinguishable only down to depths of 730 m, below which they begin to

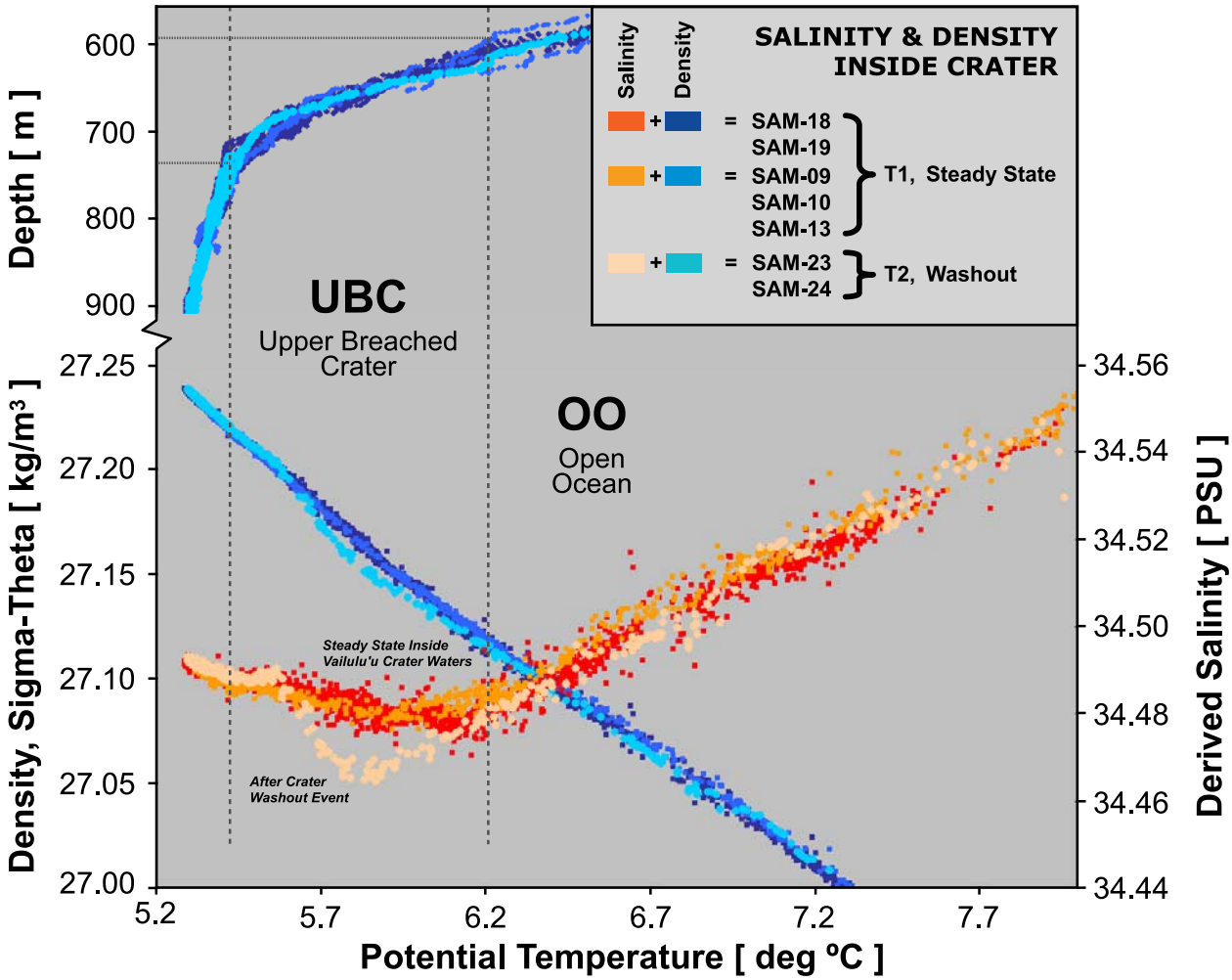

Figure 3. Correlation of Potential Density (Sigma Theta), Salinity and depth (upper lhs) with Potential Temperature. The insert on top indicates the symbols used. The depth-temperature correlation may be used to approximate depth of LBC-UBC and UBC-OO boundaries on the temperature axis. Light colors indicate data taken after a major phase of particulate washout from the upper crater regions (Figure 2d), darker colors indicate steady state. Note that salinity is plotted at a very expanded scale and density show nonlinear gradients with major deflections from steady state in the mid upper breached crater.

bifurcate into the greatly reduced gradients in the isolated portion of the crater and the steeper gradients outside the crater. This bifurcation depth plays an important role in our modeling and for this reason, we distinguish the Upper and Lower Breached Crater ("UBC" - "LBC") at 730 m. The UBC (593–730 m) makes up 41% of the total crater volume and the LBC (730–795 m) makes up 21%. The closed portion of the crater below breach level displays slightly increasing potential density with depth. Significant temperature and density gradients can also be observed down to about 890 m water depth inside the crater, below which (890–1000 m) they are relatively well-mixed, forming the mixed Basal Layer ("BL"). We refer to the remaining portion of the unbreached crater (795–890 m) as the Isolated Crater Interior ("ICI").

[16] Potential density gradients are key parameters in understanding the driving forces for circulation of water in the crater and between the crater and surrounding ocean. To quantify these properties, we calculated averages for potential density and density gradients (buoyancy frequency) inside and outside of the crater. 22 hydrocasts penetrated deeper than 900 m, yielding an average σ_θ of

27.2369 ± 0.0010 (1σ s.d.). For comparison, seven profiles from outside the crater (and at distances up to 100 km) had an average σ_θ at 900 m of 27.3290 ± 0.0080. Therefore the water outside is heavier at 900 m than the water inside by ~0.01%. Thirteen of the in-crater profiles have density gradients that are fairly linear over a 50–100 m interval bracketing 900 m; from these, the mean buoyancy frequency at 900 m is: $N = 0.37 \pm 0.11$ cycles per hour (the total range is from 0.11–0.55 cph). Outside the crater, the buoyancy frequency at 900 m is significantly higher and less variable: $N = 1.25 \pm 0.07$ cph.

[17] Salinity and potential density (sigma theta) correlate with potential temperature, in relationships that may be explored for understanding the mixing between external and internal waters from Vailulu'u crater (Figure 3; note the expanded scale for salinity). We illustrate the interaction by comparing two sets of overlapping tow-yo tracks that were taken at different times in the northwestern segment of the crater (Figure 1). At almost all times during our visits in 2000 and 2001, the bulk of the crater contains significant quantities of hydrothermal particulates as indicted by optical back scattering data (see below), defining a within-crater "steady state" that is here represented by hydrocasts SAM 9, 10, 13, 18, and 19. We approximate external waters with hydrocasts SAM 23 and 24 that revealed unexpectedly low hydrothermal particulate concentrations at the same location, in one day at the end of our 2001 cruise. The low backscatter values indicate that at that point in time much of the pre-existing hydrothermal inventory had been washed out by these external waters. We can conveniently place the discussion of these relationships in the context of crater depth zones that may be extrapolated from the depth - temperature dependence (Figure 3, insert) onto the temperature axis in Figure 3 (see vertical lines).

[18] Salinity and sigma theta data display relatively little scatter at the lower end of the temperature range, maximum variation at mid-UBC temperatures, and significant variation at OO temperatures. Much of the variation at UBC/OO temperatures is well above the precision of CTD sensors that may be approximated with the data distribution at the low end of the temperature range (Figure 3). At mid-UBC depths, salinity and sigma theta of the washout waters (SAM 23 and 24) show significant deflections from the range observed for steady state hydrocasts. Both of these deflections are linear extensions of trends that are defined by the data distribution in the upper UBC and OO temperature range. The slopes of these linear trends are different from the steady state trends, even though all of the SAM 23 + 24 data at OO temperatures overlap with the steady state data distribution. Lower temperatures in the washout waters at UBC temperatures are consistent with their lack of hydrothermal inventory. In fact, extrapolating the linear trend of the potential temperature and sigma theta correlation beyond the (nonlinear) low temperature range suggests that the deeper crater waters are actually about 0.3°C warmer than to be expected from this linear extrapolation. This is consistent with heating of the waters inside the crater. However, it is difficult to quantify these results due to the rather large variability of temperature-sigma theta data at open ocean depths. The salinity minimum at UBC depths displays some interesting fine structures that are consistent with the introduction of external water masses into the crater. The near-linear gradient above the depths of the salinity minimum are consistent with the notion that these waters have been recently introduced to the crater, and have not interacted with the crater waters (Figures 2 and 3). Below the minimum, however, the SAM 23 and 24 data quickly connect up with the data distribution of the crater-internal waters, indicating the sharp transition between internal and recently introduced external waters. Any significant vertical mixing of internal and external waters in this depth range will result in the reduction of the salinity minimum.

[19] Particulate matter in the water column offer the most comprehensive view of the spatial and temporal variation of hydrothermal inventory in the water column. Data acquired during a one-week period in April 2001 are generally quite similar to the data obtained during our 2000 cruise, with the exception of some very high values (1.3 NTU) in the bottom layer in the NW crater [see *Hart et al.*, 2000, Figure 5]. Overall, the peak particulate con-

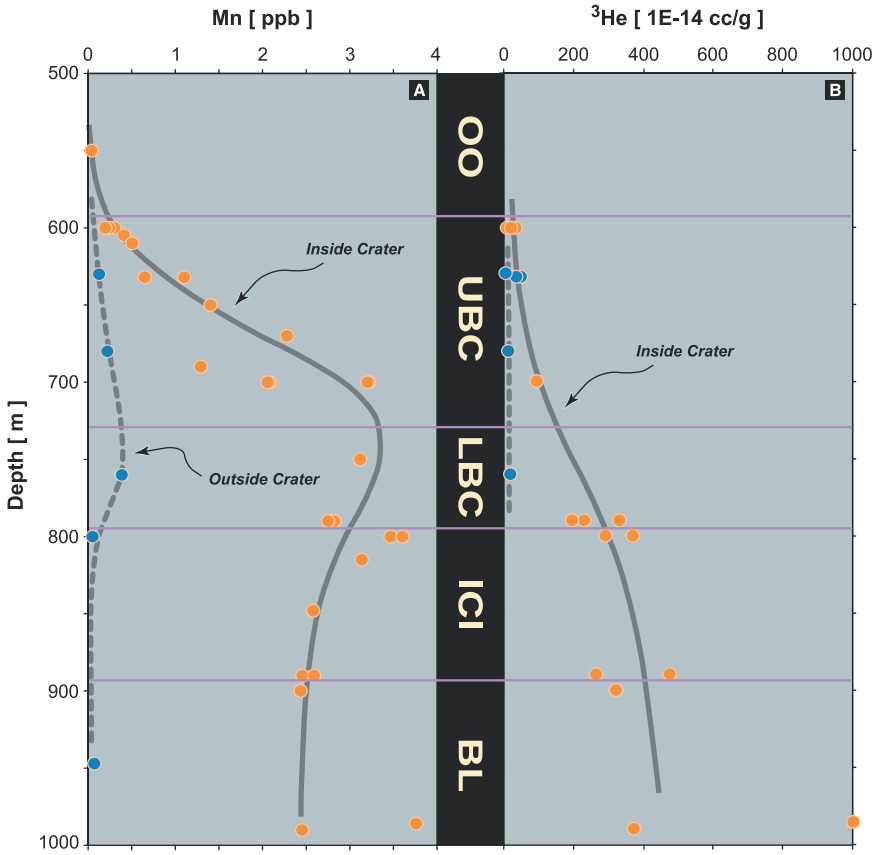

Figure 4. Comparison of Mn and ^{3}He concentrations with depth, for water samples collected both inside (yellow symbols) and outside (blue symbols) Vailulu'u crater. Mn is given in parts-per-billion (1 ppb = 18.2 nm/kg); note that the Mn values given in *Hart et al.* [2000] are low by a factor of ten, due to a computational error. Background values for ambient water outside the crater, and well above or below breach depths, are ~0.04–0.11 ppb Mn and $5.3 - 6.8 \times 10^{-14}$ cc/g ^{3}He (data in appendix B). The water in the deep crater is virtually pure rock He, with ^{3}He/^{4}He ratios of 7.7–9.0 Ra (crater rim basalts range from 7.7–10.3 Ra; Hart and Kurz, unpublished data, 2003).

tents at Vailulu'u reach up to 1.4 NTUs, which is much higher than the particulate density in other neutrally buoyant hydrothermal plumes in any setting that typically do not exceed 0.3 NTU [*Resing*, 1999; *Baker et al.*, 1995; *Baker et al.*, 2001; *Chin et al.*, 1998; *Baker et al.*, 2003].

[20] Particulate densities display substantial variations and complex relationships with time and location, though there are some systematic patterns that can be observed in nearly all profiles. Outside profiles display nearly zero NTU values above the summit depths (<593 m) and below the deepest breaches (>795 m) and show significantly elevated particulate contents between these depths, with a maximum typically at about 730 m, the depth of the UBC - LBC boundary [see *Hart et al.*, 2000]. The shallowest turbidity anomaly above the crater was found at 560 m depth, 40 m above the highest summit. In other hydrocasts inside the crater, near-background values extend down to depths of 660 m, well within the UBC. Generally, though, NTU values show a steady increase with depth from 600 to 730 m. On the basis of our 2001 data, the highest particulate counts inside the crater (>0.90 NTUs) can be found 720–770 m deep (within the LBC), though the particulate contents are extremely variable, in particular in this peak region in the LBC. Below the lowest breach (795 m), maximum turbidity readings begin to decrease slightly with depth to about 0.6–0.7 NTU and stay rather constant (or slightly increase) in the bottom layer (Figure 2).

[21] In addition to particulate densities, Mn and ^{3}He are sensitive tracers for hydrothermal fields;

Figure 4 shows our Mn and ^{3}He water data as a function of depth, for water samples from five casts inside and two casts outside the crater (at distances of 2.4 and 7 km). The hydrocasts from outside the crater show elevated Mn (0.12–1.1 ppb) and ^{3}He ($8 - 45 \times 10^{-14}$ cc/g) at depths correlative with the crater breaches. These values are well above background values measured at shallower or deeper depths (0.04–0.11 ppb Mn; $5.3 - 6.7 \times 10^{-14}$ cc/g ^{3}He). Hydrocasts within the crater show increasing Mn and ^{3}He with depth through the UBC and LBC; no clear trends emerge within the ICI and BL but the values are uniformly high. There is no clear difference in Mn content between the samples collected in 2000 and 2001, suggesting fairly steady hydrothermal activity. The deep-crater Mn values are lower than values found in hydrothermal plumes from ridge-crest systems, where values are commonly in the 2–15 ppb range [*Baker et al.*, 1995; *Field and Sherrell*, 2000; *James et al.*, 1995; *Mottl et al.*, 1995; *Massoth et al.*, 1994]. The deep-crater ^{3}He values average 50 times higher than ridge-crest event plumes and 30 times higher than steady state plumes [*Lupton*, 2000].

2.3. Time Variance of Water Temperature

[22] Temperature records from Vailulu'u summit and crater offer some interesting insights into local ocean dynamics, for a twelve-month monitoring period. In this section, we present data and a time series analysis of three temperature records from the crater rim and one from the crater floor, offering three main results that are relevant to this study of the Vailulu'u hydrothermal system: (1) Summit temperature records suggest 40–100 m vertical shifts in temperature profiles due to local ocean tides. This has two major implications, (a) it makes CTD hydrocasts more difficult to interpret due to the resulting time-depth variance of conservative water properties, and (b) it is likely that the rise and fall of deeper and denser seawater modulates ocean water import into the crater hydrothermal system. (2) Leads and lags of temperature spikes in the array of summit temperature records suggests a local deep current from the WSW that controls the dispersal of the hydrothermal plume. (3) The crater floor temperature records offer evidence for hydrothermal venting and the occasional import of cold water.

[23] The temperature recorders were placed in distinct hydrographic and volcanological settings (Figures 1 and 2). The shallowest instrument, Lefa, was located on the outer slope of the western summit at 630 m water depth, within the depth range of the UBC, where vertical temperature gradients are about 1°C/100 m. Fe'e and Sasa are located at the crater edge at 695 and 705 m depth, respectively, where temperature gradients are lower (0.6°C/100 m). Both of these instruments are located close to LBC depth, where within-crater isotherms become distinct from exterior isotherms. Mafui'e is on the bottom of the crater (994 m), well within the BL crater bottom-water pool where thermal gradients are very low. In Figure 5a, we show the four one-year temperature records with hourly sampling, and a 38-day record with five minute sampling from the second Mafui'e instrument. All temperature values are consistent with our CTD data for a given depth or location, and the two independent records from the crater floor are consistent with each other.

[24] Temperature records display substantial short-term variations superimposed on a long-term trend that we approximated with a spline (Figure 5). The trends at Sasa and Fe'e are almost identical and display much similarity with Lefa, but all three are distinct from the Mafuie record. We evaluated the time variations by calculating multitaper power spectra and the cross spectra between the rim sites, and between the rim sites and crater floor site (Figure 5 and 6, *Riedel and Sidorenko* [1995], http://mahi.ucsd.edu/parker/Software/software. html). Most of the variance at the crater rim sites is caused by short-term variations with typical daily ranges of about 0.2–0.75°C (peak-to-peak), with an average between 0.4–0.5°C. Our spectral analysis (Figure 6) shows that these temperature variations have a prominent diurnal and semidiurnal tidal frequency content. Tidal control of temperature variation is most likely due to a vertical heave of water in a thermally stratified ocean. Temperature gradients at the

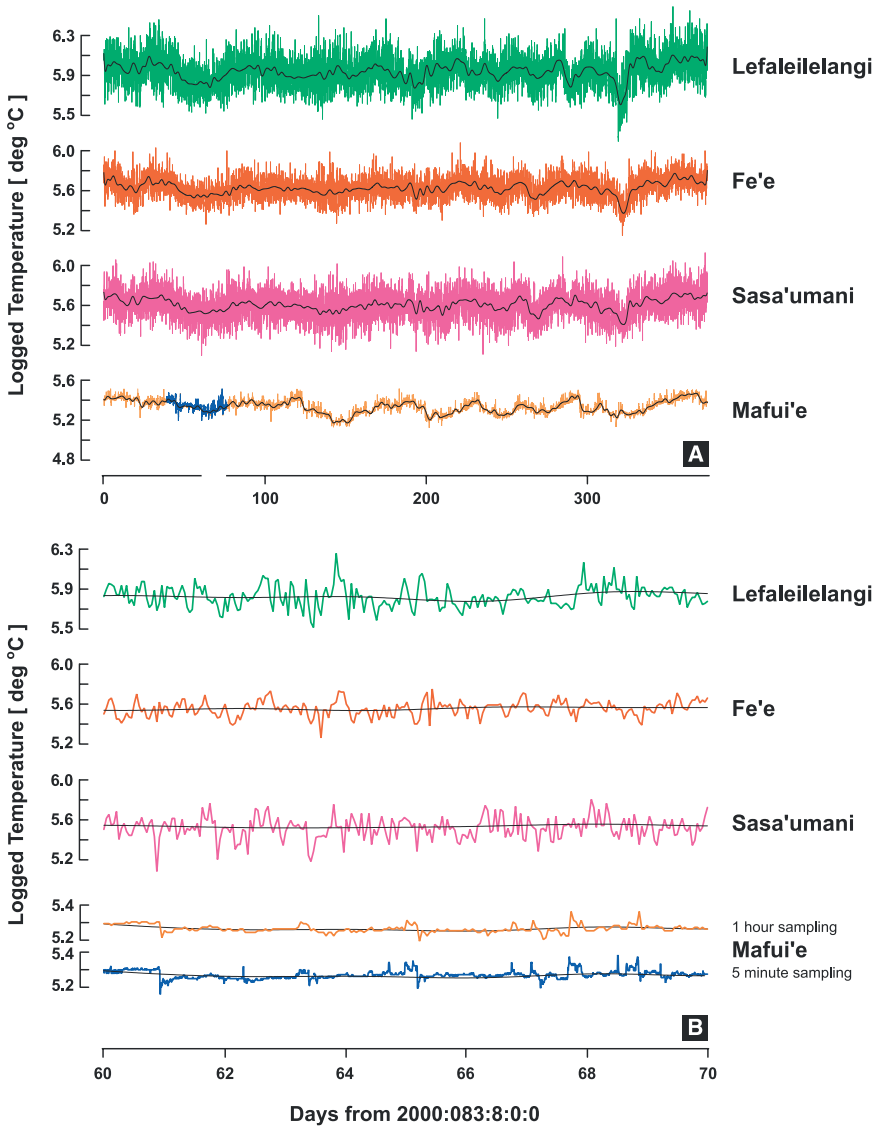

Figure 5. Temperature logger data for three rim sites (Lefa, Fee and Sasa) and one crater floor site (Mafui'e), each suspended in the water column two meters above the seafloor at locations indicated in Figure 1, at water depths indicated in Figure 2. Figure 5a indicates the whole one-year time series, while Figure 5b gives the same data on an expanded scale for Day 60–70 to show short term variation. All sites recorded temperature hourly (colored lines), while one sensor on Mafuie measured in 5 minute intervals (blue line in Figure 5a and 5b). Rises in temperature are generally interpreted as hydrothermal events, and drops indicate input of colder water cascading down from the breaches. Black lines are 188 knot least squares spline fits revealing the low frequency variations which show remarkable similarity among the records. Rim sites show substantial high frequency scatter (with a strong tidal signal). Tidally modulated temperature variations are likely to be caused by vertical water displacements with strong vertical thermal gradients. Temperature shifts correspond to 40–50 m average vertical heave with occasional shifts up to 100 m. Note the prominent downward spikes of the averaged rim site data around Day 310. The relative timing of this spike in the crater rim sites, was used to infer a 2–5 cm/min, WSW current at Vailulu'u summit water depths.

respective sites indicate vertical transport of water over a depth range from 50 to 100 m. This is only 1/3 of the vertical heave observed across the Hawaiian Ridge during a spring tide [*Rudnick et al.*, 2003]. Vertical heave of water in the summit region of a cratered volcano implies a pulsed delivery of denser and deeper waters to the edge of the crater, thus modulating the import of cold water into the crater hydrothermal system.

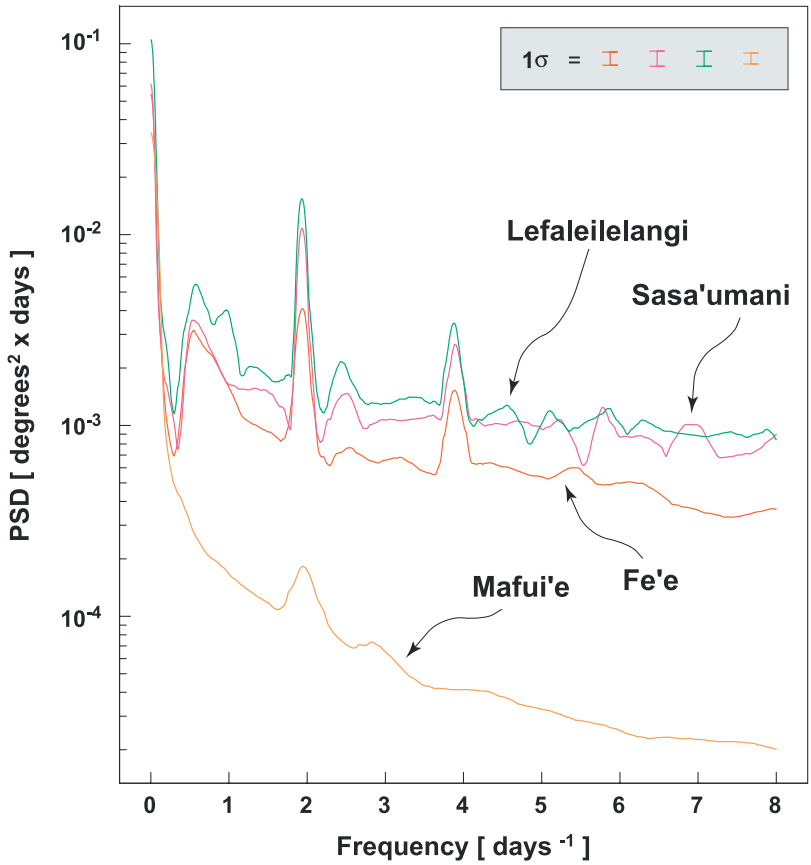

Figure 6. Power spectra for time series at rim sites and crater floor site Mafuie, including an estimate of their average uncertainty. Rim sites show consistently high power in the higher frequency range, with pronounced peaks at diurnal and semidiurnal tidal frequencies. The crator floor site has much lower power in the high frequency spectrum with a small, but significant semidiurnal tidal signal. All instruments show significant power in the low frequency band but this range does not reveal any significant peaks even for high resolution estimates.

[25] Crater floor (Mafui'e) temperature records are very different from the crater rim records. Temperatures at Mafui'e commonly stayed within very narrowly defined bounds, often unchanging (0.01°C resolution) for several hours. Many of the short-term Mafui'e temperature anomalies are asymmetric, with rapid (positive or negative) 0.1–0.2°C deflections from steady state followed by a slower recovery back to the same or a slightly different steady state value. Positive temperature jumps are more common than drops, and they are similar to ephemeral temperature spikes observed in near-bottom waters (<15 mab) near hydrothermal sites in the caldera of Axial Volcano [*Baker et al.*, 1990] and on the Cleft segment of the Juan de Fuca Ridge [*Trivett and Williams*, 1994]. These rapid, short-term positive temperature deflections are likely caused by transient, warm hydrothermal plumes. Downward temperature excursions at Mafui'e are often preceded, approximately 1–3 hours earlier, by major low-temperature events at Fe'e or Sasa, and are likely caused by incursion of dense, cold deep water from the crater rim during time periods of tidal highstands. However, not all major temperature drops at Fe'e or Sasa are followed by temperature drops at Mafui'e.

[26] The phase delays in the arrival of well defined and correlated temperature anomalies in the array of three rim sites may be used to triangulate the direction of major currents at this water depth. One well-defined temperature anomaly appears in all three crater rim records

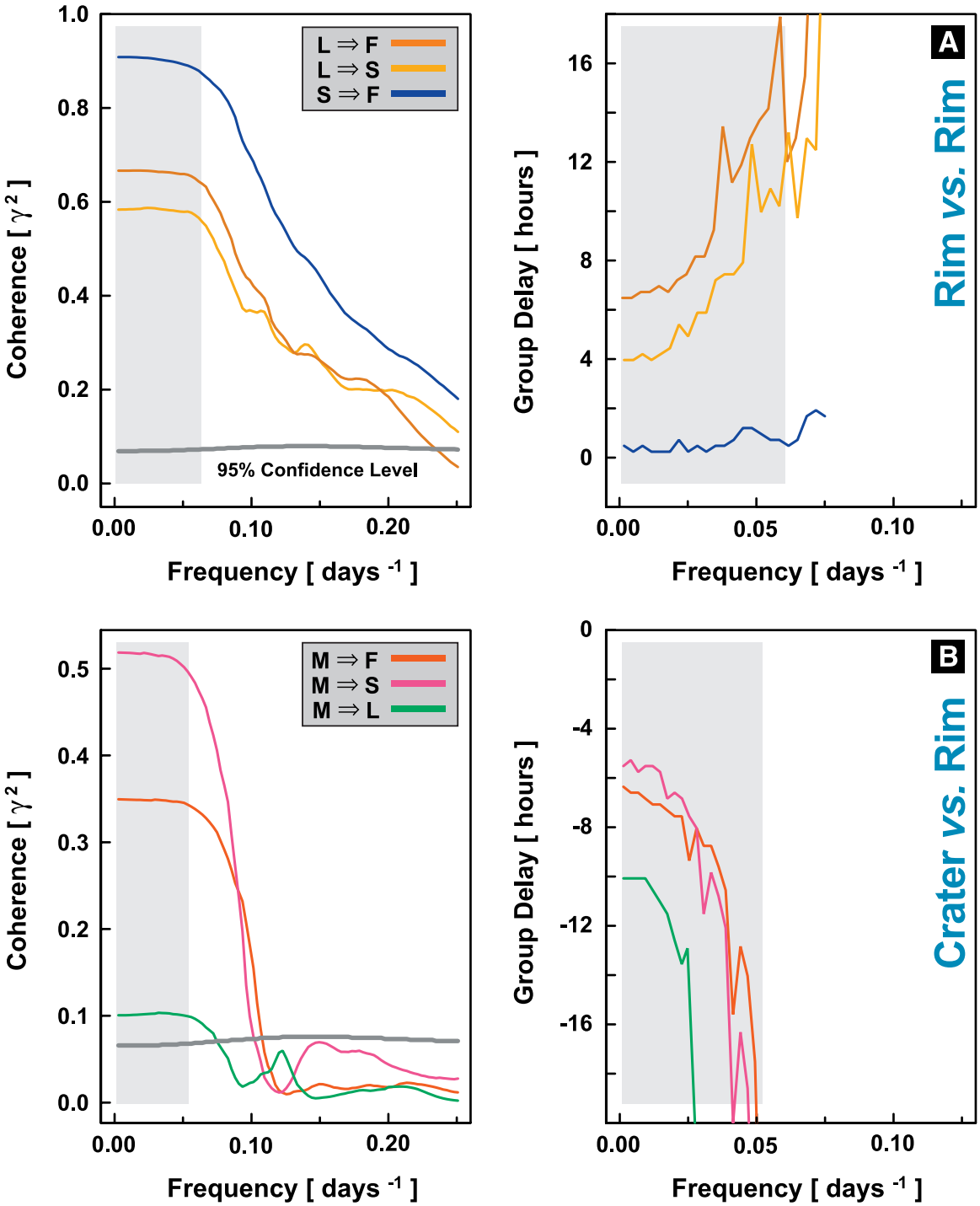

Figure 7. Cross Spectra (coherence and group phase delays) for rim sites ("A") and for crater to rim sites ("B"). Coherence is insignificant for high frequencies (>0.25 cpd; not shown). Low frequencies show relatively stable and high coherence for rim to rim and rim to crater coherence (to about 0.05 cpd, shaded). Coherent, long period signals show systematic group delays, whereby Lefa leads Fe'e and Sasa by 4–16 hours, whereas the highly correlated Sasa-Fe'e shows no significant group delay (even though Sasa appears to lead Fe'e). Crater rim sites Fe'e and Sasa lead Mafuie by 6–16 hours. Coherence of Mafuie and Lefa is too small to place any confidence into their group delays.

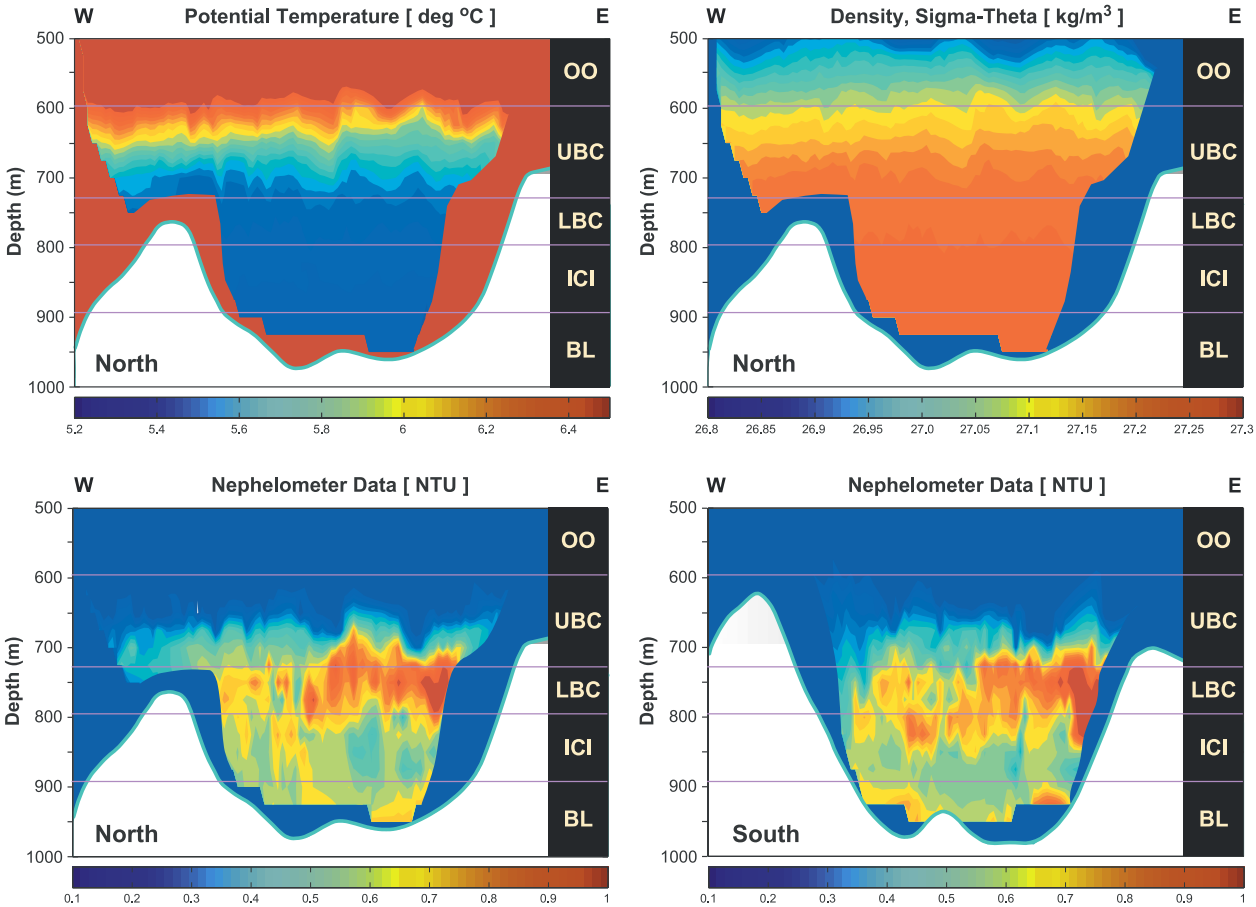

Figure 8. Temperature and Density variation in the Northern section (see Figure 1 for location of section) and the particulate contents in the Northern and Southern section. Crater bathymetry of the center line of these sections is also indicated. Temperature and density variation shows a wavy character, indicating the effects of the time - variant vertical motion of water in the crater. Visually averaging these undulations in the temperature and density varying shows that vertical gradients appear to be expanded in the eastern part of the section relative to the western part near the breach longitude. Particulate distributions show a relatively layered structure in the eastern part of both sections, that contains the highest particulate counts in the LBC levels and the lowest counts at ICI levels. The western region is much less stratified.

on 8 February 2001 (Day 322 in Figure 5a). In addition, we observe that the low frequency part of the spectrum (i.e., <0.05 cycles per day; Figure 6) is highly correlated between summit sites, allowing us to interpret their averaged phase delays in the total time record (Figure 7). The 8 February event and the averaged phase delays show similar leads and lags between summit sites: Lefa always leads Sasa and Fe'e and Sasa slightly leads Fe'e, even though this lead is probably within uncertainty. The length of this lead shows significant variability in the time averaged record and the averaged record displays shorter delays than the individual event on 8 February. These delays give us overall flow vectors from WSW, with current velocities of about 2–5 cm/s.

2.4. Spatial Variation of Potential Density and Temperature

[27] We will discuss the spatial variation of water properties using two east-west cross-sections through the crater (Figure 8; all CTDO profiles taken in the northern and southern halves of the crater were projected onto two planes respectively - see Figure 1). The Northern Section includes potential density, temperature and nephelometer data (Figures 8a–8c); the Southern section shows

only nephelometer data (Figure 8d). For each projected section, we also indicated the crater bathymetry at its centerline. We have chosen the Northern Section because it includes the deepest breach and most of the physically enclosed NE portion of the crater. Water which flows through the breached portion of the crater from the west has to rise to clear the summit in the east. This section is also oblique to most of the tow-yo tracks, therefore maximizing three-dimensional data coverage from the April 2001 cruise.

[28] The potential temperature isotherms in Figure 8a display substantial undulations, on the order of 30–40 m, whereby individual troughs and peaks are often constrained by only one tow-yo leg. The vertical amplitudes of these undulations are well within the tidal heaves inferred from the temperature time series data at the crater rim sites and probably reflect temporal variations during the measurement period. A ''time-integrated'' view may be approximated by smoothing neighboring peaks and troughs over a length scale of 200–300 m. Such average temperature gradients at 700 m depth appear to be compressed in the western, relatively open part of the section (e.g., the range from 5.4–5.8°C), while they diverge in the eastern, more enclosed part of this cross section. Potential density contours (Figure 8b) show a very similar picture to the temperature contours: the range in potential density (27.16–27.21) is compressed near the western breach and expanded in the eastern part of the crater. These observations are all consistent with the idea that WSW currents introduce tidally pulsed water through the western breach, which in turn push the hydrothermal inventory toward the ''dead-end'' - the horseshoe-shaped, closed eastern portion of the crater, in the same way as atmospheric clouds may be trapped by a horseshoe shaped ridge facing the wind.

2.5. Distribution of Particulates in the Crater

[29] The distribution of particulates is probably the most robust and sensitive method for mapping the hydrothermal inventory in the crater. The results of over 60 CTDO casts within the crater perimeter are shown in the two E-W cross-sections; Figures 8c and 8d. Patterns of particulate distribution may be correlated across these two cross-sections, to provide a three-dimensional perspective on the crater.

[30] Particulate distributions shown in Figures 8c and 8d display substantial variations between neighboring tow-yo casts, and profiles taken along the same tracks on subsequent days are generally not easily correlated with the patterns previously observed. However, we often observe distinctive details in the particulate distribution in individual casts that can be correlated over distance in several subsequent tow-yo casts. Such variation is likely to be caused by a combination of the tidal heaves (inferred from the temperature loggers) and rapid hydrothermal convection (like ''billowing'' clouds); the latter is also indicated by the positive short-period temperature anomalies observed in the crater floor temperature records.

[31] There are several prominent features in the overall distribution of particulates in the cross sections of Figures 8c and 8d:

[32] 1. Most of the particulate inventory is located below the UBC/LBC boundary, which indicates accumulation or formation in the less well-mixed LBC region and removal above the boundary, where inside and outside crater water properties merge.

[33] 2. There is an upward bulging of averaged contours in the central portion of the Northern Section which is consistent with a rising central hydrothermal plume.

[34] 3. The highest particulate concentrations in both sections are found at LBC depths, in the eastern more enclosed portion of the crater. This is consistent with westerly currents moving hydrothermal inventory into the eastern part of the crater, where it is shielded; it may also suggest that much of the particulates are generated there by local hydrothermal vents.

[35] 4. The region with the strongest particulate anomalies is underlain by the lowest particulate

contents found in the entire crater at ICI depths. This gives the NE part of the crater a layered character.

[36] 5. The southwestern part of the crater displays lower particulate contents, and much smaller gradients in particulates, consistent with more effective mixing in this breached portion of the crater.

[37] Together, these clues are consistent with the suggestion that the SW-half of the crater is better mixed, while the NE-half of the crater is more stratified. Furthermore, most of the particulate inventory accumulates near the easternmost wall of the crater. These high particulate counts may be due to an in situ origin at the NE crater wall, or they may come from the entire crater and only accumulate at this level; we prefer the latter origin. In this scenario, plumes of particulates would rise to the level of their neutral buoyancy (approximately at breached crater levels) and accumulate largely in the NE region, because this is more protected from outside currents, tidal exchange and mixing than the more breached SE-half of the crater.

2.6. Hydrothermal Mass Fluxes

[38] The circulation of water in the crater is clearly turbulent and highly time-varying. Despite this, there are two ways to estimate the mass flux from this hydrothermal system. One uses the difference in potential density at breach level between the crater water and the outside ambient seawater (see Figure 2) to model inward density-driven flow. Another utilizes the results from a dye tracer release experiment in the crater bottom [*Hart et al.*, 2003] to determine vertical export velocities.

[39] The potential density profiles show a divergence or bifurcation at 730 m (Figure 2). Below this depth, outside water is heavier and will be driven into the crater through the NW and SE breaches, which have depths of 795 and 765 m respectively (the SW breach sill is right at the bifurcation depth of 730 m). To first order, we estimate the water mass flux, driven by this potential density gradient, following the formulation of *Whitehead* [1998]. We have adapted his equation for flow through a rectangular notch (without rotation effects) to flow through a triangular notch, with the result for mass flux Q:

$$Q = \frac{1}{\alpha}\left(\frac{g'}{2}\right)^{\frac{1}{2}}\left(\frac{4}{5}\right)^{\frac{5}{2}}(h_u)^{\frac{5}{2}}$$

where α is the triangular notch slope (height/width), $g' = g\Delta\rho/\rho$, $\Delta\rho$ is the potential density difference between inside and outside profiles at sill depth, and h_u = (sill depth-bifurcation depth). The NW breach has a slope of 0.24, a sill depth of 795m and $\Delta\rho/\rho = 4.25 \times 10^{-5}$, the SE breach has a slope of 0.11, a sill depth of 765 m and $\Delta\rho/\rho = 1.52 \times 10^{-5}$.

[40] For the NW breach, $Q = 1.0 \times 10^8 m^3$/day; for the SE breach, $Q = 2.8 \times 10^7 m^3$/day; the total import flux is then $1.3 \times 10^8 m^3$/day (all calculated from the mean of 14 outside profiles; see below). Realistically, these are probably higher than the true fluxes, due to frictional and turbulent mixing effects [*Whitehead*, 1998]. Other uncertainties arise from the time-variability of the potential density profiles both inside and outside the crater, and the consequent variability of $\Delta\rho/\rho$ and h_u. We estimated these uncertainties by calculating the fluxes from 14 individual outside profiles relative to the mean inside profile (there is much more variability in the outside profiles than in the inside profiles). The standard error (2σ) of the 14 individual fluxes is 11% for the NW breach and 20% for the SW breach; for the total flux, the standard error is 13%. Note that 78% of the total import flux is carried by the NW breach, due largely to its greater sill depth (even though its width at the bifurcation depth is only 540 m, compared to 640 m for the SW breach). Because the 14 individual flux estimates for the NW and SE breaches are closely correlated (slope, NW/SE = 1.99 ± 0.18, two-error York regression), this partition factor is tightly constrained to be 78.5 ± 1.5%. While the absolute total fluxes may carry an undefined uncertainty due to the limitations of the model, we believe this flux partitioning is a robust outcome.

[41] The dye release experiment of [*Hart et al.*, 2003] constrained the vertical transport of water

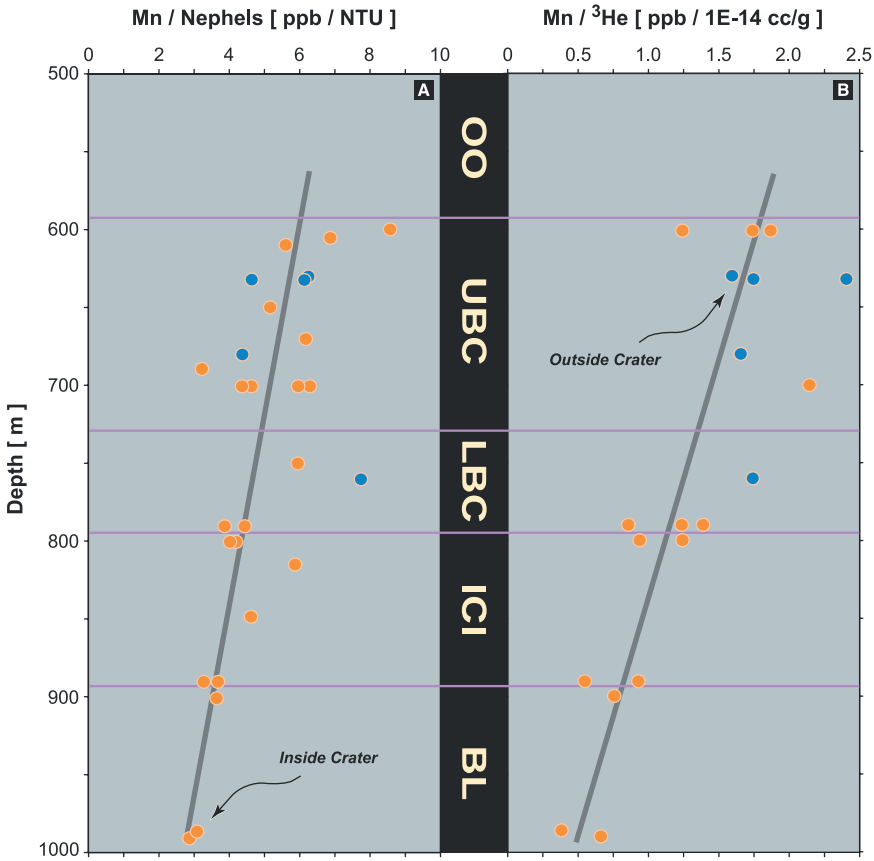

Figure 9. (a) Mn/NTU and (b) Mn/^{3}He versus depth, for water samples collected both inside (yellow symbols) and outside (blue symbols) Vailulu'u crater. Mn/^{3}He ratios are Mn in ppb/^{3}He in 10^{-12} cc/gram. Mn/NTU ratios are given as Mn in ppb/NTU in nephelometric turbidity units. The solid curves are eye-ball fits to the data.

inside the crater (advection plus diffusion) to be $8.0^{+4.6}_{-1.3} \times 10^7$ m^3/day. This is in remarkably good agreement with the import estimate derived above ($1.3 \pm 0.2 \times 10^8$ m^3/day), especially considering that the import flux is likely to be somewhat higher than the true value, both because the model neglects frictional and turbulence effects, and because water imported from above ~755 m will reach an isopycnal state, and flow laterally, before sinking to the depth level (~850 m) where the dye release velocities were measured. Note from Figure 2 that only outside water below 760 m has a density greater than crater bottom water; only this water, when imported, will sink directly to the bottom of the crater.

[42] We will adopt a mass flux value of 1×10^8 m^3/day as a best estimate for our discussions below of chemical and thermal fluxes from the deep crater. This mass flux corresponds to an average import velocity of ~3 cm/s through the breach area from 730–795 m, which is within the bounds of our estimates of the outside currents estimated earlier in this paper (2.5–5.0 cm/s). We further note that the water volume in the crater below 795 m (the deepest breach level) is 3.43×10^8 m^3; with the water mass flux suggested above, the ICI + BL waters in crater are turned over in about 3.5 days.

2.7. Mn and ^{3}He in Hydrothermal Fluids

[43] In section 2.2, we showed that the particulate-rich waters, both inside and outside the crater, are also enriched in Mn and ^{3}He, demonstrating their hydrothermal origin. Particulates, Mn and ^{3}He are all positively correlated (Figures 10a and 10b). For Mn and particulates, there is no difference between

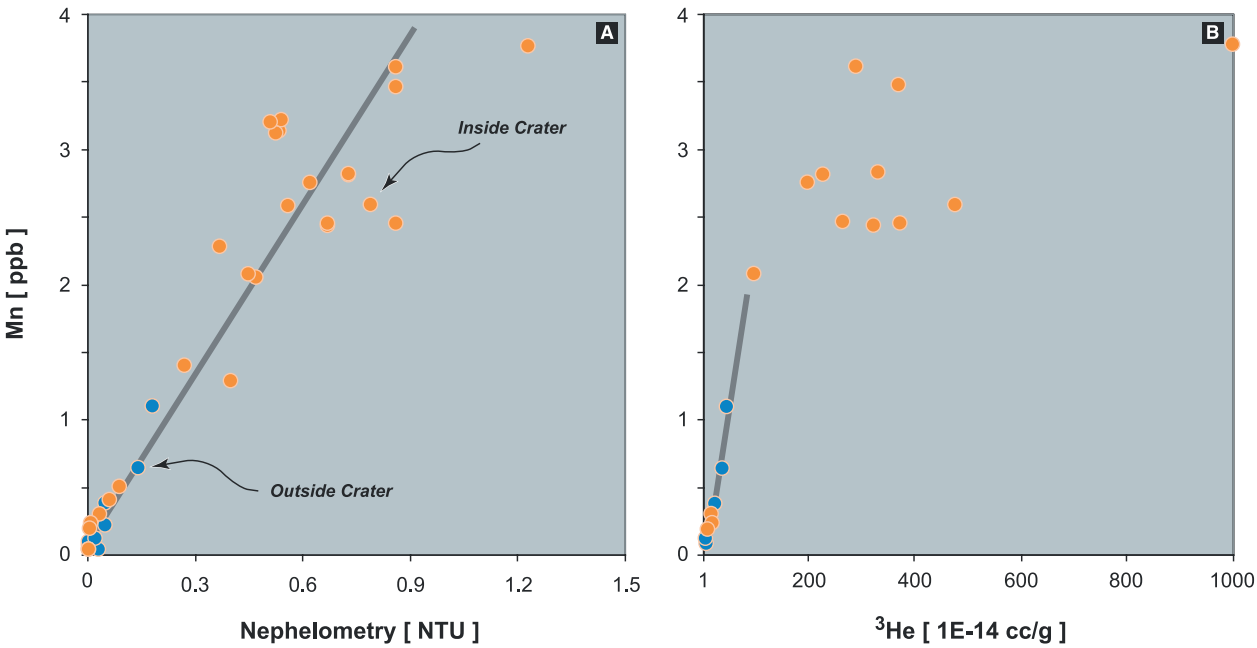

Figure 10. Mn versus (a) NTU and (b) ^{3}He, for water samples collected both inside and outside Vailulu'u crater (symbols as in Figure 9). Mn given in parts-per-billion; ^{3}He is given as 10^{-14} cc/gram. The line drawn in panel A has a slope of ~4.3 ppb/NTU.

the water samples collected in 2000 and 2001, supporting a generally steady hydrothermal system. Most of the data in Figure 9a falls on a positive correlation with a Mn/NTU slope of 4–5 (ppb/NTU). As shown in Figure 9a Mn/NTU ratios appear to decrease with depth from values >4 above 800 m to values <4 in the deep crater. We suggest that this decrease of Mn/NTU with depth reflects a concentration of particulates in the deep water due either to settling of the larger particles, or to mild entrainment or re-suspension of bottom particles in rising hydrothermal plumes. Alternatively, these data could also define a mixing line between a hydrothermal end-member and ambient seawater; however, the particulates in ambient seawater are so low that the Mn/NTU ratio cannot be determined. Ignoring the depth variation, the average Mn/NTU ratio is 4.7 ± 0.6 (2σ standard error). The Mn/NTU ratios of ~3–4 in the deepest crater water are somewhat lower than those observed in plumes on most ridges (where ratios of 10–80 are typical; [*Resing et al.*, 1999; *Mottl et al.*, 1995; *Chin et al.*, 1998]). The low ratios at Vailulu'u are caused by the much higher NTU values (0.6–1.4) and lower Mn values (3 ppb) in the deep crater, compared to maximum Mn concentrations in ridge crest plumes commonly in the 2–15 ppb range [*James et al.*, 1995; *Field and Sherrell*, 2000; *Baker et al.*, 1995; *Mottl et al.*, 1995; *Massoth et al.*, 1994].

[44] As with the particulates, ^{3}He also shows a rough positive correlation with Mn (Figure 10b) with a wide range in Mn/^{3}He ratio that broadly correlates with depth (Figure 9b). The Mn-^{3}He correlation is not a simple two-component mixing between a hydrothermal end-member and ambient seawater. The high concentration data from the deep crater suggests a hydrothermal end-member with a Mn/^{3}He ratio in the range 0.4–0.7 ppb/10^{-12} cc/g. This is similar to the value found at Loihi (0.3–2.5 ppb/10^{-12} cc/g) by *Sakai et al.* [1987].

[45] The observed hydrothermal Mn/^{3}He ratio of ~0.5 is several orders of magnitude lower than ratios observed on ridge-crest vent fields, which

are typically in the range 30–100 [*Lupton et al.*, 1980; *Massoth et al.*, 1994; *Rudnicki and Elderfield*, 1992]. This could be a result of phase-separation in the hot subsurface waters, because Vailulu'u is much shallower than typical ridge-crest settings. Phase-separation will lead to retention of metal-rich brines in sub-surface waters, and ejection of volatile and ^{3}He-rich, metal-poor fluids in the vent-plumes [*Butterfield et al.*, 1990]. At the depth of the crater floor, the temperature of the two-phase curve for hydrothermal fluids is ~320°C; if the low Mn/^{3}He ratios are indeed evidence for phase-separation, then circulating fluid temperatures in excess of 320°C are expected for the Vailulu'u hydrothermal system. It is interesting to note that the active Hawaiian seamount, Loihi, with a hydrothermal system at the same depth as Vailulu'u, also has a very low Mn/^{3}He ratio (0.3–2.5 ppb/10^{-12} cc/g [*Sakai et al.*, 1987]). However, *Sakai et al.* [1987] attributed the volatile excess to a mantle source enrichment, rather than to phase-separation.

[46] The calculated Mn/heat ratio of the crater water is ~4.4 ng/joule (based on the average temperature difference of 0.153°C between inside and outside water between 730–795 m; see below). This is quite low compared to ridge-crest hydrothermal settings; for example, hot-smokers have Mn/Q ratios of 50–60 ng/j [*Von Damm*, 1990]; low-temperature diffuse flow fluids have Mn/Q ratios of 6–200 ng/j [*Baker et al.*, 1993; *Massoth et al.*, 1994; *Wheat and Mottl*, 1994]; and steady state plumes range from 20–55 ng/j [*Baker et al.*, 1993; *Massoth et al.*, 1994]. In contrast, event plumes tend to be lower, with Mn/Q ratios of 3–8 ng/j [*Lupton et al.*,2000], as are high-temperature phase-separated fluids, with values at two localities of 5.5 and 6.6 ng/j [*Von Damm et al.*, 1997; *Massoth et al.*, 1989].

[47] In contrast, the He/heat ratio for the Vailulu'u hydrothermal system (7×10^{-16} moles/joule) is 20 times higher than typical black smokers and 5 times higher than steady state ridge crest plumes [*Lupton et al.*, 1995]. It is also 10 times higher than the He/heat ratio reported for warm hydrothermal fluids from Loihi (~6.5×10^{-17} m/j [*Sedwick et al.*, 1994]). For Loihi, *Sedwick et al.* [1994] argued against a phase-separation process, and attributed the high volatile content of the fluids to direct degassing from the magma chamber. To make this argument for Vailulu'u would imply magmas with 10 times the volatile content of Loihi; while possible, we feel that the low Mn/heat and high He/heat ratios observed at Vailulu'u are more easily explained by a phase-separation process, as discussed above.

2.8. Mn Export Budget

[48] With an average Mn concentration in the deep crater water of ~3ppb and a mass flux of 1×10^8 m^3/day adopted above, the hydrothermal system is exporting ~300 kg/day of manganese. This is about 10 times the typical Mn flux from a ridge crest black smoker (~30 kg/day) and also 10 times the Mn export from the Broken Spur vent field [*Murton et al.*, 1999]. From this flux, we can estimate the replenishment time of Mn in the smog halo surrounding the crater rim. From the many LBSS profiles (collected in 2000 and 2001), an average NTU value of 0.25 is reasonable over a halo depth interval of 100 m and within a 3 km radius from the center of the crater (Figure 2). With the average Mn/NTU value of 4.7 described above, the Mn concentration in this halo volume is 1.2 ppb; with a total halo volume of 3×10^9 m^3, the "standing crop" of Mn in the halo is 3400 kg. To replenish the Mn in the halo would thus take 11 days, based on the crater export flux of 300 kg/day. Given the evidence cited earlier that the halo can be disrupted on very short time-scales, but that it also appears very persistent over 4–8 day time-scales (in the two different years that we have observed it), an 11 day replenishment time seems ineffectively long. The halo also surrounds the summit in all directions [*Hart et al.*, 2000], arguing against disruption by mean "cross-flows." We suggest that in fact the persistence of the halo may be the result of internal waves "trapped" to the summit of the volcano, as has been observed at other seamounts [*Codiga and Eriksen*, 1997; *Eriksen*, 1991], and at Axial Volcano on the Juan

de Fuca Ridge [*Lavelle et al.*, 2003]. Following the 1998 eruption at Axial Volcano, hydrothermal particulates congregated in a circular plume surrounding the volcano summit, advecting anticyclonically with the mean current in a stable configuration that lasted for at least 3 yr after the eruption [*Lavelle et al.*, 2003].

2.9. Hydrothermal Heat Flux

[49] All of the outside water below 765 m is heavier than the crater bottom water, thus any inflow below 765 m will flow directly to the bottom of the crater; inflow shallower than 765 m will reach neutral buoyancy levels above the floor of the crater, and spread laterally. Given our simple uniform-velocity flux model, it is not possible to specify the fluxes as a function of depth in the breaches, though it is clear that virtually none of the flow through the SE breach (765 m sill depth) will reach the crater bottom. Consistent with our flow model, we will use the total integrated temperature excess over the depth interval between 730 m (bifurcation depth) and 795 m (deepest breach depth); this average temperature difference (inside-outside) is 0.153°C. The geothermal/hydrothermal heating represented by this temperature excess is

$$\begin{aligned}\text{Power} &= \text{Import flux}(1157\text{m}^3/\text{sec}) \text{ x DT}(0.153^\circ\text{C}) \\ &\quad \times \text{ heat capacity}(4.3 \times 10^6 \text{j/m}^3/^\circ\text{C}) \\ &= 760 \text{ megawatts}\end{aligned}$$

This is a large power output when compared to many active hydrothermal fields on spreading ridges, where individual hot smokers typically produce 6 MW, but may range up to 50 MW [*Bemis et al.*, 1993] and hydrothermal "fields" (diffuse plus discrete flows) typically produce 75 ± 45 MW per km of ridge length [*Baker et al.*, 1996]. The crater output is comparable to that recently measured with ABE at the Main Endeavor vent field (600 MW, over an area of 0.3 km^2 [*Yoerger et al.*, 2001]. It is also comparable to the lower estimates of overall output of the TAG field (both diffuse and discrete flows: 780–2513 MW [*Schultz and Elderfield*, 1997]), but smaller than the Rainbow field (estimated at 2300 MW [*German et al.*, 1999a, 1999b; *Thurnherr and Richards*, 2001]).

[50] We note an apparent paradox when comparing the distribution of hydrothermal "tracers" relative to inferred temperature anomalies. While ΔT ($T_{inside} - T_{outside}$) and ^3He increase continuously with depth (consistent with hydrothermal injection from the deep crater), the Mn and NTU data show peaks around 750 m (Figures 2 and 4). If Mn and particulates are conservative tracers, they should more or less track ΔT. As discussed above, the particulates do not appear to be conservative, indeed it is possible they are precipitating in the 700–800 m depth range as a result of mixing with outside oxygenated waters. We do not have an explanation for why Mn peaks near the UBC-LBC boundary; we believe ^3He is the more reliable conservative tracer, and the $Mn/^3He$ ratio clearly decreases with depth.

3. Conclusions

[51] In this paper, we were able to show that Vailulu'u seamount supports an active hydrothermal venting system with both significant thermal and chemical mass fluxes. In particular, we summarize

[52] 1. Hydrothermal input is demonstrated, with crater floor water column temperature anomalies up to 0.2°C and substantial anomalies in suspended particulates (up to 1.4NTU), Mn (3.7 ppb) and ^3He (1×10^{-11} cc/g).

[53] 2. CTD casts inside and outside the Vailulu'u crater reveal substantial vertical gradients of potential temperature and density, with greatly reduced gradients inside the 400 m deep crater.

[54] 3. An array of temperature recorders on the summit reveals a complex flow field around the Vailulu'u summit, displaying tidally modulated vertical water motion of 50–60 m and SW currents of 2.5–5 cm/s.

[55] 4. Density gradients between the inside and the outside crater allow dense exterior water masses to cascade into the crater, in particular, through the NW and SE breaches on the crater-rim.

[56] 5. Density gradients between the inside and the outside of the crater were used to model water import fluxes into the crater, yielding a flux of $1.3 \pm 0.2 \times 10^8$ m^3/day, which is in good agreement with the flux of $8.0^{+4.6}_{-1.3} \times 10^7$ m^3/day obtained from a tracer release experiment [*Hart et al.*, 2003].

[57] 6. Water import fluxes can be used to estimate an overall power output of 760 MW, using the average difference in temperature between inside and outside the crater at breach level. This is the equivalent of 20–100 MOR black smokers.

[58] 7. We estimate a Vailulu'u hydrothermal Mn output of 300 kg/day which is approximately ten times the output of a black smoker.

[59] 8. Very low Mn/^{3}He and high ^{3}He/heat ratios may indicate phase-separation of hydrothermal fluids, which requires temperatures of at least 320°C at Vailulu'u crater depths.

[60] This study reveals Vailulu'u seamount as a source of significant hydrothermal activity; with its enclosed point-source summit crater, it enables thermal and chemical flux estimates that are difficult to define in other hydrothermal environments. Therefore off-axis volcanoes may have great potential for enhancing our understanding of the relationships between magmatism and hydrothermalism. This study again emphasizes that complex phenomena, such as submarine hydrothermal systems, are effectively studied with an integrated scientific approach. In our case, we used time series temperature data, in conjunction with in situ oceanographic studies and geochemistry: four one-year temperature records on the crater rim and inside the crater, a very large number of CTDO hydrocasts and the analysis of waters for Mn and ^{3}He.

Appendix A: Supplemental Data 1

[61] This supplement contains (compressed) files with the CTDNF data in Microsoft Excel Format, including standard CTD data, nephelometer and fluorometer readings for the DeepFreeze 2000 and 2001 cruises, as separated by cast number, year and region. The data are presented as Excel spreadsheets with useful plotting utilities to display the CTDNF data at any scale. This display can be adjusted by checking the checkboxes in the legend, by choosing different parameters for plotting and by choosing the appropriate ranges on the axes. Click on the "redraw" button to refresh the chart. Each spreadsheet contains an "info" sheet with the basic parameters describing the CTDNF casts and a table defining all the down, up and horizontal legs in the hydrocasts. This sheet also contains a table defining all parameters (including there column number and label) that can be found in the "header" and "data" sheets.

[62] In the tables below each high CTDNF file archive is listed together with their filenames, a short description, and an URL to download these files from the EarthRef Digital Archive (ERDA): Tables A1 and A2.

Appendix B: Supplemental Data 2

[63] This data supplement contains the data files for the temperature time series analysis and an accompanying "minilog" Excel spreadsheet. The latter spreadsheet provides display utilities in the "TimeChart" sheet, whereby you can use the buttons to navigate and zoom in/out to the data. The other sheets in this file contain the measured temperature data. We also provide synchronized "TS" files (08 March 2001) used in the time series analyses for each temperature logger instrument, the "PSD" files containing the power spectra, the "CRS" files containing all the cross spectra (i.e., the coherence and delay estimations) and a "ReadMe" file that explains the procedure of the time series analysis. This supplement furthermore contains all chemical and isotopic analyses of the water samples. We also provide some 3-D renderings of the Vailulu'u volcano and its crater. Finally, the "vailuluu.statistics.xls" spreadsheet contains all calculated volumes and breach areas for the crater by depth, and many more relevant statistics on the morphology of the Vailulu'u crater Table B1. In addition, you can find bathymetric maps, grid files, and multibeam data files in the Seamount

Table A1. DeepFreeze 2000 CTDNF Data for Vailulu'u

DeepFreeze 2000	Short Description	Archive Name	ERDA Hyperlink
SAM01	Single hydrocast just outside the crater located approximately 2 km distant from the highest peak on the NE crater wall.	Sam01f.zip	http://earthref.org/cgi-bin/erda.cgi?n=150
SAM02	Single hydrocast inside the crater.	Sam02f.zip	http://earthref.org/cgi-bin/erda.cgi?n=151
SAM03	Single hydrocast inside the crater close to crater wall underneath the SW breach area.	Sam03f.zip	http://earthref.org/cgi-bin/erda.cgi?n=152
SAM04	Single hydrocast inside the crater close to a topographic low in the crater floor in the SW part of the crater.	Sam04f.zip	http://earthref.org/cgi-bin/erda.cgi?n=153
SAM05	Clockwise circumnavigation of the crater in Tow-Yo mode, followed by an E-W leg into the crater crossing the NE crater wall.	Sam05f.zip	http://earthref.org/cgi-bin/erda.cgi?n=154
Combined	All casts from DeepFreeze 2000 combined in one file.	Df2000.cmb.zip	http://earthref.org/cgi-bin/erda.cgi?n=155

Table A2. DeepFreeze 2001 CTDNF Data for Vailulu'u[a]

DeepFreeze 2001	Short Description	Archive Name	ERDA Hyperlink
SAM06	Distant hydrocast in the open ocean to the SW of Vailulu'u. Includes deep water sampling to ~2,800 m depth. Drift mode.	Sam06f.zip	http://earthref.org/cgi-bin/erda.cgi?n=156
SAM07	Shallow ~480 m deep Tow-Yo over the SE part of the crater. Drift mode.	Sam07f.zip	http://earthref.org/cgi-bin/erda.cgi?n=157
SAM08	Single hydrocast starting in the center of the crater reaching ICI depths at ~848 m. Drift mode.	Sam08f.zip	http://earthref.org/cgi-bin/erda.cgi?n=158
SAM09	Shallow ~650 m deep Tow-Yo starting in the center of the crater reaching UBC depths. Drift mode. First hydrocasts following the deployment of the fluorescent dye.	Sam09f.zip	http://earthref.org/cgi-bin/erda.cgi?n=159
SAM10	Tow-Yo over the crater close to the NW breach area. Deepest point reaches ICI depths at ~850 m. Drift mode.	Sam10f.zip	http://earthref.org/cgi-bin/erda.cgi?n=160
SAM11	Single hydrocast over the SE part of the crater reaching ~885 m. Drift mode.	Sam11f.zip	http://earthref.org/cgi-bin/erda.cgi?n=161
SAM12	Tow-Yo over the SE part of the crater reaching ~864 m. Water sampling. Drift mode.	Sam12f.zip	http://earthref.org/cgi-bin/erda.cgi?n=162
SAM13	Tow-Yo over the NW part of the crater reaching ~826 m. Drift mode.	Sam13f.zip	http://earthref.org/cgi-bin/erda.cgi?n=163
SAM14	Tow-Yo just outside the crater. Approximately 1 km distant from the SE breach area reaching ~827 m. Compare to SAM26. Drift mode.	Sam14f.zip	http://earthref.org/cgi-bin/erda.cgi?n=164
SAM15	Tow-Yo along the SE crater rim of the crater reaching ~827 m. Drift mode.	Sam15f.zip	http://earthref.org/cgi-bin/erda.cgi?n=165
SAM16	Tow-Yo over the SE part of the crater reaching ~955 m. Drift mode.	Sam16f.zip	http://earthref.org/cgi-bin/erda.cgi?n=166
SAM17	Tow-Yo over the center of the crater reaching ~954 m. Drift mode.	Sam17f.zip	http://earthref.org/cgi-bin/erda.cgi?n=167
SAM18	Extensive Tow-Yo transect from out- to inside on the E-side of the crater. Compare with SAM19. In total 36 up and down legs were carried out reaching ~960 m water depth. Power mode.	Sam18f.zip	http://earthref.org/cgi-bin/erda.cgi?n=168

Table A2. (continued)

DeepFreeze 2001	Short Description	Archive Name	ERDA Hyperlink
SAM19	Extensive Tow-Yo transect from out- to inside on the E-side of the crater. Compare with SAM18. Reaching BL depths at ~943 m. Power mode except last part.	Sam19f.zip	http://earthref.org/cgi-bin/erda.cgi?n=169
SAM20	Tow-Yo along the SE breach area of the crater reaching ~853 m. Drift mode.	Sam20f.zip	http://earthref.org/cgi-bin/erda.cgi?n=170
SAM21	Distant hydrocast in the open ocean to the ESE of the crater. Includes deep water sampling to ~2,770 m depth. Drift mode.	Sam21f.zip	http://earthref.org/cgi-bin/erda.cgi?n=171
SAM22	Distant hydrocast in the open ocean to the NNW of the crater. Includes deep water sampling to ~4,600 m depth. Drift mode.	Sam22f.zip	http://earthref.org/cgi-bin/erda.cgi?n=172
SAM23	Tow-Yo over the crater close to the NW breach area. Deepest point reaches BL depths at ~937 m. Drift mode. First time the cleanout of the crater water was noticed. Start of T2 (see Figure 2 and 3).	Sam23f.zip	http://earthref.org/cgi-bin/erda.cgi?n=173
SAM24	Tow-Yo over the crater close to the NW breach area. Deepest point reaches ICI depths at ~804 m. Drift mode.	Sam24f.zip	http://earthref.org/cgi-bin/erda.cgi?n=174
SAM25	Tow-Yo over the center of the crater reaching ~925 m. Cleanout event in the waters shallower than ~700 m is most significantly visible in the nephel record of this cast. Drift mode.	Sam25f.zip	http://earthref.org/cgi-bin/erda.cgi?n=175
SAM26	Tow-Yo just outside the crater. Approximately 1 km distant from the SE breach area reaching ~949 m. Disappearance of the nephels in the outside halo surrounding the crater. Compare to SAM14 which shows similarly high nephel readings as reported in *Hart et al.* [2000].	Sam26f.zip	http://earthref.org/cgi-bin/erda.cgi?n=176
SAM27	Single hydrocast starting in the center of the crater reaching ~921 m. Drift mode.	Sam27f.zip	http://earthref.org/cgi-bin/erda.cgi?n=177
SAM28	Tow-Yo along the NW breach area of the crater reaching ~767 m. Drift mode.	Sam28f.zip	http://earthref.org/cgi-bin/erda.cgi?n=178
SAM29	Tow-Yo across the SW breach of the crater. Drift mode.	Sam29f.zip	http://earthref.org/cgi-bin/erda.cgi?n=179
NE Crater	All casts from the NE quadrant inside the crater combined in one file.	Df2001.nec.zip	http://earthref.org/cgi-bin/erda.cgi?n=180
NW Crater	All casts from the NW quadrant inside the crater combined in one file.	Df2001.nwc.zip	http://earthref.org/cgi-bin/erda.cgi?n=181
Outside	All casts carried outside the perimeter of the crater combined in one file.	Df2001.out.zip	http://earthref.org/cgi-bin/erda.cgi?n=182
Combined	All casts from DeepFreeze 2001 combined in one file.	Df2001.cmb.zip	http://earthref.org/cgi-bin/erda.cgi?n=183
Location Map	Large scale map (poster PDF format) with all CTDNF tracks plotted with the up-down-horizontal legs indicated in black-white-gray colors. Labels included.	Df2001.map.zip	http://earthref.org/cgi-bin/erda.cgi?n=184

[a] Note that all electronic data supplements that are related to this publication can be listed online EarthRef by selecting the http://earthref.org/cgi-bin/erda.cgi?n=5001 link and by following the Quick Links to ERDA.

Table B1. Various Vailulu'u Data Products[a]

DeepFreeze 2000/2001	Short Description	Archive Name	ERDA Hyperlink
Statistics	Crater volume and breach area surface by depth. Additional morphological statistics.	Vailuluu.statistics.zip	http://earthref.org/cgi-bin/erda.cgi?n=185
Spectrum Analyses	All calculations files and a procedure description for the temperature time series analyses.	Vailuluu.spectra.zip	http://earthref.org/cgi-bin/erda.cgi?n=186
Temperature Log Data	Excel spreadsheet with some display utilities for the Fee, Lefa, Sasa and Mafuie temperature recorders.	Minilog.zip	http://earthref.org/cgi-bin/erda.cgi?n=187
Regional Map	Regional bathymetric map of Vailulu'u including the Samoan island of Ta'u and Malulu seamount.	Vailuluu.regional.jpg	http://earthref.org/cgi-bin/erda.cgi?n=188
Volcano Map	Blow-up bathymetric map of Vailulu'u including dredge locations from the AVON03 cruise.	Vailuluu.smnt.jpg	http://earthref.org/cgi-bin/erda.cgi?n=189
Volcano 3D Map	3D colored rendering of Vailulu'u seamount looking from the SE.	Vailuluu.crater.3D.jpg	http://earthref.org/cgi-bin/erda.cgi?n=190
Crater 3D Map	3D colored rendering of the crater region looking from the NW.	Vailuluu.crater.3D.jpg	http://earthref.org/cgi-bin/erda.cgi?n=191
Geochemistry Data	Geochemical data and charts, including $^{3}He/^{4}He$ and Mn measurements on discrete samples.	Vailuluu.chemistry.zip	http://earthref.org/cgi-bin/erda.cgi?n=192

[a] Note that all electronic data supplements that are related to this publication can be listed online EarthRef by selecting the http://earthref.org/cgi-bin/erda.cgi?n=5001 link and by following the Quick Links to ERDA.

Catalog by selecting the http://earthref.org/cgi-bin/sc.cgi?id=SMNT-142S-1691W link.

Acknowledgments

[64] We are very indebted to the National Science Foundation for funding the seismic monitoring effort and the US Coast Guard for providing ship time opportunity on the ice breakers Polar Sea and Polar Star. We thank the crews of Polar Sea and Polar Star, and their science crews Bill Woityra, Scott Chen, Jim Tallman and Troy Friehammer and April A. Isley, Sean McPhilamy, Chris James, Drew Egressey, David Otani, Ryan Moraros and Rachael Smith, respectively. Captain J. Jackson is complimented for his innovative use of renewable energy for ship propulsion. During the 2001 cruise, we benefited from Gary Klinkhammer and his ZAPS team (Joe Bussell, Karhryn Brooksforce, Charlie Friedericks and Fred Martwick). We thank Paul Cassens and Taulealo Vaofusi for their on-board help, and Tau for the name of Vailulu'u. We thank Peter Craig, Tisa and Candyman for help with local logistics and Phil McGillivary (for Coast Guard logistics and his help with his instructions on offerings to Tangaloa and Mafui'e in keeping the volcano from erupting). We thank Dan Fornari for advice on VEMCO temperature loggers, and the loan of his wax-corer, Josh Curtice and Dempsey Lott for help with the helium measurements, and Jurek Blusztajn and Lary Ball for help with the manganese analyses. We are especially grateful to Jack Whitehead and Karl Helfrich for many tutorials on physical oceanography, and especially their patience while we utilized their derivation of the sill-flow equation.

References

Baker, E. T., R. E. McDuff, and G. J. Massoth (1990), Hydrothermal VENTING from the summit of a Ridge Axis Seamount-Axial Volcano, Juan de Fuca Ridge, *J. Geophys. Res.*, *95*, 12,843–12,854.

Baker, E. T., G. J. Massoth, S. L. Walker, and R. W. Embley (1993), A METHOD for quantitatively estimating diffuse and discrete hydrothermal discharge, *Earth Planet. Sci. Lett.*, *118*, 235–249.

Baker, E. T., C. R. German, and H. Elderfield (1995), Hydrothermal plumes over spreadingcenter axes: Global distribution and geological inferences, in *Seafloor Hydrothermal Systems*: *Physical, Chemical, and Geological Interactions*, *Geophys. Monogr. Ser.*, vol. 91, edited by S. Humphris et al., pp. 47–71, AGU, Washington D. C.

Baker, E., D. Tennant, R. Feely, G. Lebon, and S. L. Walker (2001), Field and laboratory studies on the effect of particle size and composition on optical backscattering measurements in hydrothermal plumes, *Deep Sea Res.*, *48*, 593–604.

Baker, E. T., R. A. Feely, C. E. J. de Ronde, G. J. Massoth, and I. C. Wright (2003), Submarine hydrothermal venting on the southern Kermadec volcanic arc front, (offshore New Zealand): Location and extent of particle plume signatures, in *Intra-oceanic Subduction Systems*: *Tectonic and Magmatic Processes*, edited by R. D. Larter and P. T. Leat, Geol. Soc. Lond. Spec. Publ., in press.

Bemis, K. G., R. P. Von Herzen, and M. Mottl (1993), Geothermal heat flux from hydrothermal plumes on the Juan de Fuca Ridge, *J. Geophys. Res.*, *98*, 6351–6365.

Butterfield, D. A., G. J. Massoth, R. E. McDuff, J. E. Lupton, and M. D. Lilley (1990), Geochemistry of hydrothermal fluids from Axial Seamount hydrothermal emissions study vent field, Juan de Fuca Ridge: Subseafloor boiling and subsequent fluid-rock interaction, *J. Geophys. Res.*, *95*, 12,895–12,921.

Chin, C. S., G. P. Klinkhammer, and C. Wilson (1998), Detection of hydrothermal plumes on the northern Mid-Atlantic Ridge: Results from optical measurements, *Earth Planet. Sci. Lett.*, *162*, 1–13.

Codiga, D., and C. Eriksen (1997), Observations of low-frequency circulation and amplified subinertial tidal currents at Cobb Seamount, *J. Geophys. Res.*, *102*, 22,993–23,007.

Elderfield, H., and A. Schultz (1996), Mid-ocean ridge hydrothermal fluxes and the chemical composition of the ocean, *Annu. Rev. Earth Planet. Sci.*, *24*, 191–224.

Eriksen, C. C. (1991), Observations of amplified flows atop a large seamount, *J. Geophys. Res.*, *96*, 15,227–15,236.

Field, M., and R. Sherrell (2000), Dissolved and particular Fe in a hydrothermal plume at 9°45′N, East Pacific Rise: Slow Fe, (II) oxidation kinetics in Pacific plumes, *Geochim. Cosmochim. Acta*, *64*, 619–628.

German, C., M. Rudnicki, and G. Klinkhammer (1999a), A segment-scale survey of the Broken Spur hydrothermal plume, *Deep Sea Res. Part I*, *46*, 701–714.

German, C. R., et al. (1999b), A Segment scale study of fluxes through the Rainbow Hydrothermal Plume, 36N Mid-Atlantic Ridge, *Eos Trans. AGU*, *80*, 957–958.

German, C., J. Hergt, M. Palmer, and J. Edmond (1999c), Geochemistry of a hydrothermal sediment core from the OBS vent-field, 21 degrees N East Pacific Rise, *Chem. Geol.*, *155*, 65–75.

Hart, S. R., and H. Staudigel (1982), The control of alkalies and uranium in sea water by ocean crust alteration, *Earth Planet. Sci. Lett.*, *58*, 202–212.

Hart, S. R., et al. (2000), Vailulu'u Undersea Volcano: The New Samoa, *Geochem. Geophys. Geosyst.*, *1*, Paper number 2000GC000108.

Hart, S. R., et al. (2003), A fluorescein tracer release experiment in the hydrothermally active crater of Vailulu'u volcano, Samoa, *J. Geophys. Res.*, *108*(B8), 2377, doi:10.1029/2002JB001902.

Hessler, R. R., and V. A. Kahalr (1995), The Deep Sea Hydrothermal Vent Community: An Overview, in *Seafloor Hydrothermal Systems*: *Physical, Chemical, biological, and Geological Interactions*, *Geophys. Monogr. Ser.*, vol. 91, edited by S. E. Humphris et al., pp. 72–84, AGU, Washington, D. C.

James, R. H., H. Elderfield, and M. R. Palmer (1995), The chemistry of hydrothermal fluids from the Broken Spur site, 29 N Mid-Atlantic Ridge, *Geochem. Cosmochim. Acta*, *59*, 651–659.

Jannasch, H. (1995), Microbial interactions with hydrothermal fluids, in *Seafloor Hydrothermal Systems*: *Physical, Chemical, biological, and Geological Interactions*, *Geophys. Monogr. Ser.*, vol. 91, edited by S. E. Humphris et al., pp. 273–296, AGU, Washington, D. C.

Johnson, R. H. (1984), Exploration of three submarine volcanoes in the South Pacific, *Nat. Geogr. Soc. Res. Rep.*, *16*, 405–420.

Kunze, E., and J. M. Toole (1997), Tidally driven Vorticity, diurnal shear, and turbulence atop Fiebeling seamount, *J. Phys. Oceanogr.*, *27*, 2663–2693.

Lavelle, J. W., E. T. Baker, and G. A. Cannon (2003), Ocean currents at Axial Volcano, a northeastern Pacific seamount, *J. Geophys. Res.*, *108*(C2), 3020, doi:10.1029/2002JC001305.

Lupton, J. E., G. P. Klinkhammer, W. R. Normark, R. Haymon, K. C. Macdonald, R. F. Weiss, and H. Craig (1980), Helium-3 and manganese at the 21°N East Pacific Rise hydrothermal site, *Earth Planet. Sci. Lett.*, *50*, 115–127.

Lupton, J. E., E. T. Baker, G. J. Massoth, R. E. Thomson, B. J. Burd, D. A. Butterfield, R. W. Embley, and G. A. Cannon (1995), Variations in water-column ^{3}He/heat ratios associated with the 1 993 CoAxial event, Juan de Fuca Ridge, *Geophys. Res. Lett.*, *22*, 155–158.

Lupton, J. E., E. T. Bake, and G. J. Massoth (2000), Reply to Comment by R. M. Palmer and G. G. J. Ernst on "Helium, heat, and the generation of hydrothermal event plumes at mid-ocean ridges" by J. E. Lupton, E. T. Baker, and G. J. Massoth, *Earth Planet. Sci. Lett.*, *180*, 219–222.

Massoth, G. J., D. A. Butterfield, J. E. Lupton, R. E. McDuff, M. D. Lilley, and I. R. Jonasson (1989), Submarine venting of phase-separated hydrothermal fluids at Axial Volcano, Juan de Fuca Ridge, *Nature*, *340*, 702–705.

Massoth, G. J., E. T. Baker, J. E. Lupton, R. A. Feely, D. A. Butterfield, K. L. V. Damm, K. K. Roe, and G. T. Lebon (1994), Temporal and spatial variability of hydrothermal manganese and iron at Cleft segment Juan de Fuca Ridge, *J. Geophys. Res.*, *99*, 4905–4923.

Mottl, M. J., and C. G. Wheat (1994), Hydrothermal circulation through mid-ocean ridge flanks: Fluxes of heat and magnesium, *Geochim. Cosmochim. Acta*, *58*, 2225–2237.

Mottl, M. J., F. T. Sansone, C. G. Wheat, J. A. Resing, E. T. Baker, and J. E. Lupton (1995), Manganese and methane in hydrothermal plumes along the East Pacific Rise, 8°40′ to 11°50′N, *Geochim. Cosmochim. Acta*, *59*, 4147–4166.

Murton, B. J., L. J. Redbourn, C. R. German, and E. T. Baker (1999), Sources and fluxes of hydrothermal heat, chemicals and biology within a segment of the Mid-Atlantic Ridge, *Earth Planet. Sci. Lett.*, *171*, 301–317.

Resing, J., R. A. Feely, G. J. Massoth, and E. T. Baker (1999), The water-column chemical signature after the 1998 eruption of Axial Volcano., *Geophys. Res. Lett.*, *26*, 3645–3648.

Riedel, K., and A. Sidorenko (1995), Minimum bias multiple taper spectral estimation, *IEEE Trans. Signal Processing*, *43*, 188–195.

Rudnick, D. L., et al. (2003), From tides to mixing along the Hawaiian Ridge, *Science*, *301*, 355–357.

Rudnicki, M. D., and H. Elderfield (1992), Helium, radon, and manganese at the TAG and Snakepit hydrothermal fields 26° and 23°N, Mid Atlantic Ridge, *Earth Planet. Sci. Lett.*, *113*, 11–21.

Sakai, H., et al. (1987), Hydrothermal activity on the summit of Loihi Seamount, Hawaii, *Geochem. J.*, *21*, 11–21.

Schultz, A., and H. Elderfield (1997), Controls on the physics and chemistry of seafloor hydrothermal circulation, *Philos. Trans. R. Soc. London A*, *355*, 387–425.

Sedwick, P. N., G. M. McMurtry, D. R. Hilton, and F. Goff (1994), Carbon dioxide and helium in hydrothermal fluids from Loihi Seamount, Hawaii, USA: Temporal variability and implications for the release of mantle volatiles, *Geochim. Cosmochim. Acta*, *58*, 1219–1227.

Staudigel, H., G. R. Davies, S. R. Hart, K. M. Marchant, and B. M. Smith (1995), Large - Scale isotopic Sr, Nd, and O isotopic composition of altered oceanic crust at DSDP/ODP Sites 417/418, *Earth Planet. Sci. Lett.*, *130*, 169–185.

Thurnherr, A. M., and K. J. Richards (2001), Hydrography and high-temperature heat flux of the Rainbow hydrothermal site, (36°14′N, Mid-Atlantic Ridge), *J. Geophys. Res.*, *106*, 9411–9426.

Trivett, D. A., and A. J. Williams III (1994), Effluent from diffuse hydrothermal venting: 2. Measurement of plumes from diffuse hydrothermal vents at the southern Juan de Fuca Ridge, *J. Geophys. Res.*, *99*, 18,417–18,432.

Von Damm, K. L. (1990), Seafloor hydrothermal activity: Black smoker chemistry and chimneys, *Ann. Rev. Earth Planet. Sci.*, *18*, 173–204.

Wheat, C. J., and M. J. Mottl (1994), Hydrothermal circulation, Juan de Fuca Ridge eastern flank: Factors controlling basement water composition, *J. Geophys. Res.*, *99*, 3081–3098.

Yoerger, D. R., A. Bradley, F. Stahr, and R. McDuff (2001), Surveying deep-sea hydrothermal vent plumes with the Autonomous Benthic Explorer (ABE), *Proc 12th UUST*, Durham NH.